

Creative Commons Attribution 4.0 International (CC BY 4.0)

<https://creativecommons.org/licenses/by/4.0/>

Access to this work was provided by the University of Maryland, Baltimore County (UMBC) ScholarWorks@UMBC digital repository on the Maryland Shared Open Access (MD-SOAR) platform.

Please provide feedback

Please support the ScholarWorks@UMBC repository by emailing scholarworks-group@umbc.edu and telling us what having access to this work means to you and why it's important to you. Thank you.



Jupiter's Banding and Jets May Be Caused by Tides

Robert H. Tyler^{1,2}

¹ Geodesy and Geophysics Laboratory, NASA Goddard Spaceflight Center, Greenbelt MD 20771, USA

² GESTAR II, University of Maryland Baltimore County, MD 21250, USA; rtyle@umbc.edu

Received 2022 June 1; revised 2022 August 15; accepted 2022 August 31; published 2022 November 7

Abstract

The stratification parameters for Jupiter's outer 3000 km shell are calculated using a density profile recently derived from observations of the NASA Juno spacecraft currently in Jovian orbit. Using these parameters, the equations of classical tidal theory for a stratified, nonhydrostatic, compressible fluid are numerically solved for sectoral tidal forcing by Io. The results support a long-standing though little discussed proposal that the banding/jets (and possibly the unexplained endogenic heat) are caused by the tides. First, general arguments from eigenmode analyses expect resonantly forced tidal modes and the scattering of the tidal response to higher spatial degrees by Jupiter's fast rotation, with time-averaged tidal effects appearing in bands between critical latitudes ($\pm 50^\circ$ for forcing by Io). Second, resonant tides and banding are specifically demonstrated in the tidal model configured with the Juno-derived stratification. While banding in the time-averaged tidal features is a robust expectation (from the well-prescribed forcing and rotation parameters) and is independent of the internal parameters, the details of the banding (e.g., number, width) are highly dependent. Hence, comparison of the tidal model with observations provides a test of the tidal hypothesis of the bands as well as assumptions of interior parameters and processes. Here, dissipation parameterized as a simple pressure relaxation term in the vertical balance equation shows a time-mean banded structure between the critical latitudes that can drive geostrophic jets matching the major observed features, including strong prograde flow at the equator. By contrast, alternate stratification/dissipation assumptions produce banded structures that do not agree with observations.

Unified Astronomy Thesaurus concepts: Jupiter (873); Hot Jupiters (753); Solar system gas giant planets (1191); Atmospheric tides (118); Tides (1702)

1. Introduction

For more than a century, there has been speculation that Jupiter's tides may be resonantly forced and responsible for the observed banding. As reported in Whitmell (1899), M. Souleyre affirmed that the belts on Jupiter are due to the satellites, but provided no supporting computations. When the "highest authority on tides" G. H. Darwin (son of Charles) was consulted on the matter, he pointed to the expected "kinetic augmentation" of the tides due to Jupiter's rapid rotation. Finally, the prominent pioneer in terrestrial atmospheric tidal theory, R. Lindzen, appears to have independently proposed the role of resonant dynamic tides and banding on Jupiter (Lindzen 1991), and this was followed with further calculations (Lindzen 1991; Ioannou & Lindzen 1993a, 1993b, 1994). Recently, the inviscid eigenmodes reported in Ioannou & Lindzen (1993a) were confirmed in Tyler (2019a, 2019b), a domain of millions of tidal solutions spanning different input and dissipation process assumptions was constructed and analyzed, and it was concluded that Jupiter's tidal response very likely includes resonantly forced modes and intense rotational scattering (Tyler 2019b).

Surprisingly, these previous works have received little review or mention when discussing tides or the dynamics of banding, despite that modern reviews still describe the bands as a major unresolved problem in the dynamics of planetary atmospheres (Ingersoll et al. 2004; Sánchez-Lavega 2011) and despite the importance of understanding the tidal response in

interpreting data from the Juno mission in progress. Juno tidal models currently assume nondynamic equilibrium-tide states (Wahl et al. 2016, 2020), or dynamically perturbed states for an adiabatic interior (Idini & Stevenson 2021). Neither are appropriate for the stratified outer shell. These Juno tide model studies do not consider nor even cite the papers described in the last paragraph. The goal of this paper is to provide a simplified description and extension of the most compelling points of the tidal banding hypothesis and to provide tidal model results explicitly demonstrating these effects, thereby indicating that they need to be considered in interpreting Juno data as well as more generally in studies of the tidal dynamics of fast-rotating stratified fluids.

There are then two types of calculations in this paper that distinguish it from other approaches in Juno tide modeling: (1) the use of the full equations of classical tidal theory (CTT) to estimate the tidal response in the stratified outer layer of Jupiter; (2) the demonstration of bands and jets generated by time-mean effects (e.g., dissipative heating) of these tides. For calculating the tidal response in Jupiter's outer layers, justification for using the CTT equations has already been described in the Lindzen and Ioannou papers cited, and here complete solutions to these equations are obtained using a validated methodology. By contrast, the correct dynamical tide solution for this application (i.e., of tides in the stratified outer layer) would not be obtained by the formulations used in the Juno tidal models cited above because approximations in the equations either remove important inertial terms (Wahl et al. 2016, 2020) or make simplifying (though unproven) assumptions regarding an adiabatic/unstratified interior (Idini & Stevenson 2021). While these other tidal models may be accurate for some components of the tidal response, it is already clear from the approximations in their



Original content from this work may be used under the terms of the [Creative Commons Attribution 4.0 licence](https://creativecommons.org/licenses/by/4.0/). Any further distribution of this work must maintain attribution to the author(s) and the title of the work, journal citation and DOI.

starting equations that they cannot model dynamic tides in the upper stratified layer considered here. Regarding the calculation of banding and jets, the approach here is distinct of course because other Juno work does not consider the tides as the source. In reviewing the potential explanations for the bands and jets, three different types of processes are described in Ingersoll et al. (2004). The tidal hypothesis is indeed mentioned but only in a short paragraph that does not reach any conclusion nor present or cite any follow-up studies of the original work. The other two potential explanations are reviewed much more extensively. In one, the bands are regarded as surface expressions of axis-aligned Taylor columns (which would be hard to support with stratification). The other, which most work has followed in variations, involves the rectification of turbulent momentum by spin into latitudinal bands. It is not in the goal or scope of the work here to vet these other explanations beyond noting that despite the years of work, results have not provided a widely accepted explanation for the bands/jets, and there have also been, in cases, inconsistencies of the models with observations (e.g., prograde equatorial flow, and the number and long-term stability of the bands).

While confidence in detailed estimates of Jupiter’s tidal response calculated using the CTT equations is indeed limited by uncertainties in prescribing its internal parameters and processes, there are elements of the tidal-response results that are robustly compelling because they come solely or primarily from the well-known rotation and tidal-force parameters rather than the internal assumptions. One robust expectation is that Jupiter’s fast rotation will scatter the tidal response across spatial scales; the spherical-harmonic degree-two tidal forces will excite not just a degree-two response but rather a spectrum of degrees of the same parity. A related expectation is that time-mean effects of the tides will appear as banded structures between “critical latitudes” where the local Coriolis frequency matches that of the specific tidal forcing, causing a dynamical transition between wavelike and evanescent character. The strongest tidal forces are due to Io, and the force frequency is dependent on the difference between Io’s orbital period and Jupiter’s rotation rate. The predicted critical latitudes are then specifically $\pm 50^\circ$ and independent of internal parameters. Another robust expectation is that even with relatively weak dissipation, dynamic tides in Jupiter’s atmosphere can plausibly account for all or part of Jupiter’s unresolved endogenic heating (taken here to be 7.5 W m^{-2} , on average, following Li et al. 2018) and possibly the rapid lifting of Io’s orbit (Lainey et al. 2009).

Further constraints on the expected tidal behavior can be obtained by combining theoretical arguments with observational data, including data newly available from Juno. This study considers tides generated in the outer $\sim 3000 \text{ km}$ shell above the ohmic drag expected in the conductive deeper layers and below the cloud/weather layers starting at 100 bar. Under the tidal hypothesis, the banding and jets are driven by time-mean effects of the tides, and an important result from Juno is that the jets appear to extend deeply through this outer shell (Kaspi et al. 2018; Duer et al. 2020; Galanti & Kaspi 2021). It has usually been assumed that the interior (below some shallow surface layer with radiative cooling) is adiabatic because of convection driven by a deeper endogenic heat source. Here, this assumption must be relaxed to allow for the possibility of significant heat due to tides in the outer shell. A corollary is that the outer shell may be stratified throughout its depth. Recently, a study of Juno gravity data has provided a density profile of

Jupiter’s interior that may provide observational support for deep stratification through this shell (the result varies with the assumed adiabatic index Γ_1). In Appendix B.1, the density data in Ni (2018) is combined with the vertical balance equations (assuming the value $\Gamma_1 = 2$) and the calculated buoyancy frequency shows stable stratification throughout the shell, albeit decreasing quickly from the surface.

The observational evidence of banding on Jupiter is clear, and the number of bands plausibly follows from basic estimates of stratification in the outer layer and tidal theory (Lindzen 1991). However, for spherically symmetric interior properties (though Juno gravity and magnetic data already preclude this as a strict assumption), the dominant sectoral tidal forces of the satellites should create only latitudinally symmetric features, while the observed jets include asymmetry and possibly even some degree of antisymmetry. The tesseral tidal forces (dependent on the orbital inclination of the moon) would indeed create antisymmetric features. The tidal response due the weaker tesseral forces (as well as the forces by the more distant moons) were considered in Tyler (2019b). It was shown that because of resonant amplification, these weaker forces can in fact lead to the dominant tidal response but only in rather slender sections of the solution domain involving specific internal parameters that would likely occur only locally within the radially varying range in Jupiter. Hence, it is expected that the observable bulk tidal effects are driven by the stronger sectoral tides of Io considered in this study. That said, as these weaker forces also have higher critical latitudes, their tides and dynamical boundaries might be seen in polar regions where they do not overlap with that of the sectoral tides (Tyler 2019b). Further, observational studies of ammonia concentration in the upper atmosphere implicating equatorial (possibly banded) vertical velocities (Ingersoll et al. 2017) might be driven by either bulk or locally generated tidal heat. Because the stratification parameters vary with depth, different modes are excited at different depths with an associated variation in the number and thickness of the bands of time-averaged tidal effects. Vertical propagation, wave interference, and boundary conditions are also important in the vertical structure of the tidal response, and the largest-scale eigenmodes tend to be trapped rather than vertically propagating (see Appendix B.4). The distinction of the propagating modes was critical in the earlier tidal studies where it was not known that the jets extend deeply. Vertical propagation could bring tidal momentum from a stratified interior (where the higher density allows more work) up to drive jets at the surface.

This study aims to demonstrate and understand bulk time-mean tidal effects extending deeply through the outer shell. The model for driving the jets differs from that of the previous studies. As the banding and jets will arrive in a wide range of conceivable models, the model here is intended to be simple and illustrative. The calculated tidal dissipation (parameterized through a pressure relaxation term in the vertical balance equation) is depth averaged and then regarded as a heat/pressure source driving geostrophically balanced flow. Because the tidal dissipation is depth-dependent, one could seek to model the depth dependence for the jets. This is, however, not warranted here because the crude dissipation assumed obviously parameterizes an unresolved process. Realistic pressure losses of the tides would likely first propagate vertically and redistribute before being converted to the heat/pressure driving the jets. While the tides calculated in Tyler (2019b) were essentially two-dimensional (modal or equivalent

Table 1
Definitions of the Basic Operators and Parameters

	Dimensional	Nondimensional
partial time derivative operator (1/s)	∂_t	$\tilde{\partial}_t = (2\Omega_s)^{-1}\partial_t$
horizontal gradient operator (1/m)	∇_H	$\tilde{\nabla}_H = (1/r)^{-1}\nabla_H$
horizontal divergence operator (1/m)	$\nabla_H \cdot$	$(1/r)^{-1}\tilde{\nabla}_H \cdot$
horizontal Laplacian operator (1/m ²)	∇_H^2	$\tilde{\nabla}_H^2 = (1/r^2)^{-1}\nabla_H^2$
Coriolis parameter (1/s)	f	$\tilde{f} = (2\Omega_s)^{-1}f$
rotation rate (1/s)	Ω	$\tilde{\Omega} = (\Omega_s)^{-1}\Omega$
horizontal flow velocity (m/s)	\mathbf{u}_H	$\tilde{\mathbf{u}}_H = (G_s/(2\Omega_s r))^{-1}\mathbf{u}_H$
vertical flow velocity (m/s)	w	$\tilde{w} = (G_s/(2\Omega_s r))^{-1}w$
total force vector (N/m ³)	\mathbf{F}_H	$\tilde{\mathbf{F}}_H = (\rho_0 G_s/r)^{-1}\mathbf{F}_H$
prescribed force vector (N/m ³)	$\mathbf{F}_H^{(p)}$	$\tilde{\mathbf{F}}_H^{(p)} = (\rho_0 G_s/r)^{-1}\mathbf{F}_H^{(p)}$
frequency (1/s)	ω	$\tilde{\omega} = (2\Omega_s)^{-1}\omega$
dissip. coef. for divergent flow (1/s)	$\alpha_{d,b}$	$\tilde{\alpha}_{d,b} = (2\Omega_s)^{-1}\alpha_{d,b}$
dissip. coef. for rotational flow (1/s)	$\alpha_{r,b}$	$\tilde{\alpha}_{r,b} = (2\Omega_s)^{-1}\alpha_{r,b}$
dissip. coef. for vertical balance (1/s)	α_p	$\tilde{\alpha}_p = (2\Omega_s)^{-1}\alpha_p$
longitudinal wavenumber	s	s
dissipation timescale (s)	$T_{(j)}$	$\tilde{T}_{(j)} = (\tilde{\alpha}_{(j)})^{-1} \tilde{\omega} $
wave speed (m/s)	c_e	$\tilde{c}_e = (2\Omega_s r)^{-1}c_e$
slowness (s/m)	ν	$\tilde{\nu} = (2\Omega_s r)\nu$
dynamic pressure (N/m ²)	p	$\tilde{p} = (\rho_0 G_s)^{-1}p$
gravitational potential (m ² /s ²)	\mathfrak{G}	$\tilde{\mathfrak{G}} = (G_s)^{-1}\mathfrak{G}$
work density (W/m ³)	\mathcal{W}	$\tilde{\mathcal{W}} = (\rho_0 G_s^2/(2\Omega_s r^2))^{-1}\mathcal{W}$
dissipation density (W/m ³)	\mathcal{D}	$\tilde{\mathcal{D}} = (\rho_0 G_s^2/(2\Omega_s r^2))^{-1}\mathcal{D}$
power density (W/m ³)	\mathcal{P}	$\tilde{\mathcal{P}} = (\rho_0 G_s^2/(2\Omega_s r^2))^{-1}\mathcal{P}$
pressure-source term (1/s)	\mathfrak{s}	$\tilde{\mathfrak{s}} = \left(\frac{G_s}{2\Omega_s r^2}\right)^{-1}\mathfrak{s}$

Note. Here, r is the radius, and $\rho_0 = \rho_0(r)$ is the background density distribution. Nondimensionalization introduces the arbitrary scaling factors Ω_s (with units of s⁻¹), and $G_s = G_s(r)$ (with units of m² s⁻²). In studies such as this one involving nonzero rotation and gravitational forcing, we assign $\Omega_s = \Omega$, and $G_s = |\mathfrak{G}(r)|$.

barotropic) or incomplete (estimated from the particular solution, which could be obtained despite uncertain internal structure), the complete three-dimensional solutions calculated here using the Juno-derived stratification provide stronger support for resonant tides and banding in Jupiter.

To meet the goals described, the main text is kept short and focused on first presenting simplified theoretical arguments for the expectation of rotational scattering and resonantly forced states (Section 2), and following with the explicit demonstration of these tidal effects as well as time-mean bands and jets in a three-dimensional numerical tidal model (Section 3). Details of the numerical methodology are reviewed in Appendix A, with the model input parameters and configuration for the Jovian application described in Appendix B. The several analytical methods for obtaining tidal-response solutions described in Appendix C support Section 2 and are also useful in providing exact solutions to idealized cases. These solutions

explicitly show the dependencies on input parameters, and they were also used to validate the numerical model. The appendices also include methodological components and results that will be useful in extending the study to describe the tidal response beyond the elements that are the focus of this study.

2. Theoretical Discussion

Here a simplified discussion is given of CTT and behavior, with an emphasis on understanding the conditions necessary for resonantly forced states and rotational scattering. The operators, variables, and parameters are defined in Tables 1, 2, and 3, and follow the detailed derivations developed for the Tidal Response Of Planetary Fluids (TROPF) software package. (A summary of the TROPF formulation and solution approach is provided in Appendix A). The notation of operators \mathcal{L} anticipate their conversion to matrices L operating on a vector of spherical-

Table 2

Operators Used in the Governing Equations (where I Is the Identity Operator, θ Is Colatitude, and the Other Parameters Are Defined in Table 1)

Suboperators:
$\mathcal{L}_L = [\tilde{\nabla}_H^2]$
$\mathcal{L}_C = \left[\tilde{\Omega} \cos \theta \tilde{\nabla}_H^2 + \tilde{\Omega} \sin^2 \theta \frac{\partial}{\partial \cos \theta} \right]$
$\mathcal{L}_{\tilde{\alpha}_d} = [\Sigma_b \tilde{\alpha}_{d,b} \tilde{\nabla}_H^{2b}]$
$\mathcal{L}_{\tilde{\alpha}_r} = [\Sigma_b \tilde{\alpha}_{r,b} \nabla_H^{2b}]$
\mathcal{L}_V (see the text)
Composite operators:
$\mathcal{L}_A = [[\tilde{\omega} + i\mathcal{L}_{\tilde{\alpha}_d}]\mathcal{L}_L - s\tilde{\Omega}]$
$\mathcal{L}_B = [[\tilde{\omega} + i\mathcal{L}_{\tilde{\alpha}_r}]\mathcal{L}_L - s\tilde{\Omega}]$
$\mathcal{L}_H = [[-\mathcal{L}_L^{-1}][\mathcal{L}_A - \mathcal{L}_C \mathcal{L}_B^{-1} \mathcal{L}_C][\tilde{\omega} \mathcal{L}_L^{-1}]$
$\mathcal{L}_{\tilde{p}} = [I - \mathcal{L}_H \mathcal{L}_V]$

Table 3

Matrices (L) Representing the Operators (\mathcal{L}) in Table 2 as Used in the TROPF Spherical-harmonic Method

Suboperators:
$L_L = \text{diag}(-\mathbf{n}(\mathbf{n} + 1))$
$L_C = \text{diag}_{(-1)}\{-\tilde{\Omega}\mathbf{n}(\mathbf{n} + 2)(\mathbf{n} - s + 1)/(2\mathbf{n} + 1)\}$ $+ \text{diag}_{(+1)}\{-\tilde{\Omega}(\mathbf{n} - 1)(\mathbf{n} + 1)(\mathbf{n} + s)/(2\mathbf{n} + 1)\}$
$L_{\tilde{\alpha}_d} = \Sigma_b \tilde{\alpha}_{d,b} \text{diag}\{(-\mathbf{n}(\mathbf{n} + 1))^b\} = \Sigma_b \tilde{\alpha}_{d,b} L_L^b$
$L_{\tilde{\alpha}_r} = \Sigma_b \tilde{\alpha}_{r,b} \text{diag}\{(-\mathbf{n}(\mathbf{n} + 1))^b\} = \Sigma_b \tilde{\alpha}_{r,b} L_L^b$
$L_V = \text{diag}\{(\tilde{v}^2)_{\mathbf{n}}^s\}$ (see the text for nondiagonal form)
Composite operators:
$L_A = [[\tilde{\omega} + iL_{\tilde{\alpha}_d}]L_L - s\tilde{\Omega}]$
$L_B = [[\tilde{\omega} + iL_{\tilde{\alpha}_r}]L_L - s\tilde{\Omega}]$
$L_H = [[-\mathcal{L}_L^{-1}][L_A - L_C L_B^{-1} L_C][\tilde{\omega} L_L^{-1}]$
$L_{\tilde{p}} = [I - L_H L_V]$

Note. Here \mathbf{n} is a column vector of degrees $n = s, s + 1, \dots, N_{\text{trunc}}$. “diag” indicates that the vector argument is placed on the main diagonal of a square matrix, while “diag₍₋₁₎”, “diag₍₊₁₎” indicate placement on the first lower and first upper subdiagonals, respectively (the last vector element is clipped in the case of the lower diagonal, and the first element is clipped in the case of the upper diagonal). Analytical inverses of all of the submatrices are obtained by taking the reciprocal of the diagonal entries, with the exception of the nondiagonal matrix L_C and possibly L_V .

harmonic coefficients. Governing composite operators (some emphasized with brackets $[\cdot]$ operating on operands $\{\cdot\}$) are efficiently constructed from factorized suboperators. The derivation of the vertical operator \mathcal{L}_V follows Tyler (2019a, 2019b) and is summarized in Appendix A.1. While the notation and compact formulation here are unconventional, the underlying equations (with some minor extensions for versatility) for both the horizontal and vertical structure are identical to those previously described in CTT (e.g., Auclair-Desrotour et al. 2016)

and specifically applied to Jupiter (Lindzen 1991; Ioannou & Lindzen 1993a, 1993b, 1994).

As shown in detail in Tyler (2019a, 2019b) and summarized in Appendix A, the equations of CTT can be combined into a single equation,

$$\mathcal{L}_{\tilde{p}} \tilde{p} = \tilde{\Theta}, \quad (1)$$

governing the nondimensional reduced pressure \tilde{p} , where $-\tilde{\Theta}$ is the time-dependent gravitational potential.

For this discussion, it is helpful to expand $\mathcal{L}_{\tilde{p}}$ in terms of differential operators \mathcal{L}_H , \mathcal{L}_V acting with respect to horizontal and vertical coordinates, respectively, such that (1) becomes

$$[I - \mathcal{L}_H \mathcal{L}_V][\tilde{p}] = \tilde{\Theta}. \quad (2)$$

In the more traditional canonical form, the governing equations of CTT are presented as a system of first-order equations involving more than one variable. These can be combined into a higher-order equation for one of a choice of variables including the vertical velocity, divergence, and the Helmholtz potentials for the horizontal velocity. The choice here where the variable is \tilde{p} is useful because we wish to understand what controls tidal power and resonance. The work performed on the fluid depends only on the coupling of \tilde{p} and $\tilde{\Theta}$ and can be described as simply

$$\tilde{\mathcal{W}} = \tilde{\Theta} \mathcal{L}_V \tilde{\partial}_t \tilde{p}. \quad (3)$$

Under the assumption of an energy balance, the time/globe averaged work $\tilde{\mathcal{W}}$ and dissipation $\tilde{\mathcal{D}}$ rates are equivalent and can be referred to as the average tidal power $\tilde{\mathcal{P}}$.

Resonantly forced tidal states are high-power states where the energy transferred from the system’s orbit/spin to the fluid is elevated above what might be expected from simple scaling estimates. The governing form in Equation (2) is convenient as it can be immediately combined with Equation (3) to write the solution for work as

$$\tilde{\mathcal{W}} = \tilde{\Theta} \mathcal{L}_V [I - \mathcal{L}_H \mathcal{L}_V]^{-1} \{\tilde{\partial}_t \tilde{\Theta}\}, \quad (4)$$

where it has been assumed that the parameters in \mathcal{L}_H and \mathcal{L}_V are independent of time. In essence, maximally amplified resonant tides can occur when $\|\mathcal{L}_H \mathcal{L}_V\| \approx I$, where I is the identity operator. By contrast, the so-called “equilibrium tide” is achieved when $\|\mathcal{L}_H \mathcal{L}_V\| \ll I$. In this case $\tilde{p} \approx \tilde{\Theta}$ and $\tilde{\mathcal{W}} = \tilde{\Theta} \mathcal{L}_V \{\tilde{\partial}_t \tilde{\Theta}\}$. The quadrature phase in the $\tilde{\Theta}$ product shows that in the equilibrium case of periodic tides, the time-averaged work over a tidal cycle will be zero provided the operator \mathcal{L}_V (and \mathcal{L}_H) remains real, as will be the case without dissipation terms.

Toward more general analytical solutions, note that the formulation in Equation (4), or more fundamentally Equation (2), has a form that is ideal in that it immediately allows the solution to be expressed as a series using a Neumann expansion of the operator. For example, when $\|\mathcal{L}_H \mathcal{L}_V\| < I$, the analytical solution to (4) can be written as

$$\tilde{\mathcal{W}} = \tilde{\Theta} \mathcal{L}_V \sum_{j=0}^{\infty} [\mathcal{L}_H \mathcal{L}_V]^j \{\tilde{\partial}_t \tilde{\Theta}\}. \quad (5)$$

(As described further in Appendix C.1, a related analytical series solution is available for the case where $\|\mathcal{L}_H \mathcal{L}_V\| > I$.) This is regarded as an analytical solution, as it involves only the repeated differential operation $[\mathcal{L}_H \mathcal{L}_V]$ and summation of terms, but not the integration or inversion implicit in $[I - \mathcal{L}_H \mathcal{L}_V]^{-1}$.

The analytical solution is also insightful because the terms in the series describe the physical effects of rotation and of fluid wave speeds when they are too slow to establish a quasistatic balance with forces. The first term ($j=0$) describes the equilibrium tide already discussed. The $j>0$ terms then describe the modifications due to the slow response of the fluid and the scattering of energy across spatial scales due to rotation. The scattering by rotation is important and not necessarily intuitive to those working with tides in planetary solids or viscous fluids. While the scattering can be seen in the definition of \mathcal{L}_H , it is perhaps more clear to see in the associated matrix operator L_H acting on the vector of spherical-harmonic coefficients. As seen in Table 3, L_H is composed of factorized suboperator matrices. All of the suboperators are diagonal with the exception of L_C , which involves only the first sub- and superdiagonals. One sees that L_C also vanishes when there is no rotation ($\tilde{\Omega} \rightarrow 0$). L_H involves applying L_C twice with the result that L_H is a tri-diagonal matrix involving the diagonal and the second sub- and superdiagonals. This couples degree n with degrees $n \pm 2$ assuring scattering across degrees of the same (even or odd) parity. By contrast, scattering can be negligible when the rotation rate is much smaller than either the forcing frequency or the inverse dissipation timescale.

Not surprisingly, the same analytical solutions above indicate that for highly resonant conditions ($\mathcal{L}_H \mathcal{L}_V \rightarrow I$), the series will converge slowly or even diverge. While the solutions for Jupiter to be discussed are obtained using TROPF, which by design does not have the limitation of restrictions on $\|\mathcal{L}_H \mathcal{L}_V\|$, it is insightful to further consider analytical solutions following a different approach. Let the μ th eigenvalue of \mathcal{L}_H be $\tilde{c}_{e,(\mu)}^2$, and the λ th eigenvalue of \mathcal{L}_V be $\tilde{v}_{(\lambda)}^2$. The conditions for resonance are that for some pair μ, λ there be the relationship $\tilde{v}_{(\lambda)}^2 \approx \tilde{c}_{e,(\mu)}^2$, and that there be, of course, a nonvanishing projection of the forcing onto the horizontal/spatial forms of the associated eigenfunctions such that these resonant modes can be excited. For a fast rotator like Jupiter, the last condition is not as restrictive as it might first appear because the dominant degree-two tidal force will be projected across a wide range of eigenmodes (by contrast, for idealized slow-rotators, the eigenfunctions converge with spherical harmonics and the force projection becomes limited). So the more important condition is probably the first one. A complete expansion of the solution in terms of the $\tilde{p}_{(\mu,\lambda)}$ eigenmodes provides an algebraic solution method for obtaining solutions $\tilde{p}_{(\mu,\lambda)}$ to forcing $\tilde{\mathfrak{G}}_{(\mu,\lambda)}$ provided the eigenmodes of both \mathcal{L}_H and \mathcal{L}_V (or of $\mathcal{L}_H \mathcal{L}_V$) are known. Alternatively, one can expand in terms of just one of the operators and solve the resulting differential equation for each (μ th or λ th) mode. Because the \mathcal{L}_H eigenmodes are insensitive to internal parameter assumptions, it is efficient to solve the differential equation for each of the μ modes as described in Appendix C.2 (the homogeneous solutions obtained are also useful in describing which modes will propagate vertically).

While these analytical expansion methods are useful for gaining theoretical insight, in the TROPF calculations presented in this study, neither expansion is needed as the governing matrix operator $L_{\tilde{p}}$ is represented in a block-diagonal supermatrix holding positions for each of the spherical-harmonic coefficients at each of the radially discretized layers. Although $L_{\tilde{p}}$ is then extremely large, it is also

very sparse, and the three-dimensional tidal solution is instantly obtained using a direct solver.

The operators \mathcal{L}_H and \mathcal{L}_V can, when reduced to less general forms than represented in TROPF, be related to previous descriptions. When dissipation terms are removed from the horizontal momentum equations and g is assumed constant, \mathcal{L}_H^{-1} becomes the more traditional “Laplace tidal operator” with associated “Hough” eigenfunctions and eigenvalues that can be represented as nondimensional squared wave speeds or (assuming constant gravity) equivalent depths (Hough 1898). When the dissipation/relaxation and source/heating terms are removed, \mathcal{L}_V used in this study follows from the same underlying equations assumed in Lindzen (1991) and Ioannou & Lindzen (1993a, 1993b, 1994) for a stratified, nonhydrostatic, compressible fluid. When dissipation/relaxation and pressure-source/heating terms are included but specifically modeled as Newtonian cooling and heat sources, then \mathcal{L}_V is constructed from the same underlying equations as in Auclair-Desrotour et al. (2016). While \mathcal{L}_H and the traditional Laplace tidal operator \mathcal{L}_H^{-1} have the same set of eigenvalues (in fact, the case of tides by Io on Jupiter is specifically used as a validation of the TROPF software by showing that the eigenvalues of L calculated with TROPF agree with those previously calculated for L_H^{-1} in Ioannou & Lindzen 1993a), the associated operator L_H used in TROPF has the advantage of being an easily coded tri-diagonal matrix that is computationally efficient because explicit calculation of the inverse (L_H^{-1} , a full matrix) is not required.

Finally, physical intuition can be distilled from the notes above. In the condition for a resonant mode (considered here as $[I - \mathcal{L}_H \mathcal{L}_V] \rightarrow (1 - \tilde{c}_{e,(\mu)}^2 \tilde{v}_{(\lambda)}^2) \approx 0$ and momentarily assuming each of $\tilde{c}_{e,(\mu)}^2$ and $\tilde{v}_{(\lambda)}^2$ are real and positive), $\tilde{c}_{e,(\mu)}^2 \tilde{v}_{(\lambda)}^2$ may be regarded as an adjustment index expressing the squared ratio of the force-dependent configurational wave speed $\tilde{c}_{e,(\mu)}$ and the wave speed $\tilde{v}_{(\lambda)}^{-1}$ at which the fluid can adjust to the pressure disturbance. (In the case of a barotropic, or equivalent barotropic, fluid, the single mode \tilde{v}^{-1} is just the prescribed shallow-water wave speed.) For more general situations with dispersion and dissipation, $\tilde{v}_{(\lambda)}$ is referred to as the slowness. In frequency-domain studies, this can also be related to a complex vertical wavenumber. From a rough estimate of the range of Jupiter’s expected stratification, it was argued in Tyler (2019b) that there should be multiple modes $\tilde{v}_{(\lambda)}^2$ that overlap with $\tilde{c}_{e,(\mu)}^2$ such that $\tilde{c}_{e,(\mu)}^2 \tilde{v}_{(\lambda)}^2 \approx 1$ (this can now be shown explicitly using the eigenvalues of \mathcal{L}_V used in this study). Hence, the solution method must allow for layers that are resonantly forced.

An imaginary component of the index $\tilde{c}_{e,(\mu)}^2 \tilde{v}_{(\lambda)}^2$ represents attenuation, and this cancels the possibility of unbound resonant amplitudes. Dissipation (e.g., drag) in \mathcal{L}_H leads to an imaginary component of $\tilde{c}_{e,(\mu)}^2$, while dissipation in \mathcal{L}_V (e.g., Newtonian cooling, or the simpler pressure relaxation assumed in this study) leads to an imaginary component of $\tilde{v}_{(\lambda)}^2$. With very small fluid slowness (or, alternatively, the smaller spatial scales implicit in a small $\tilde{c}_{e,(\mu)}$), there is fast adjustment and the equilibrium solution $\tilde{p}_{(\mu,\lambda)} = \tilde{\mathfrak{G}}_{(\mu,\lambda)}$ is reached. With very large fluid slowness, $\tilde{p}_{(\mu,\lambda)} = (-\tilde{c}_{e,(\mu)}^2 \tilde{v}_{(\lambda)}^2)^{-1} \tilde{\mathfrak{G}}_{(\mu,\lambda)}$, and $\tilde{p}_{(\mu,\lambda)}$ is 180° out of phase with $\tilde{\mathfrak{G}}_{(\mu,\lambda)}$. When dissipation is so large that the index is primarily imaginary, $\tilde{p}_{(\mu,\lambda)}$ is 90° out of phase with $\tilde{\mathfrak{G}}_{(\mu,\lambda)}$. Without an imaginary component in this index, there is no time/globe averaged work or dissipation.

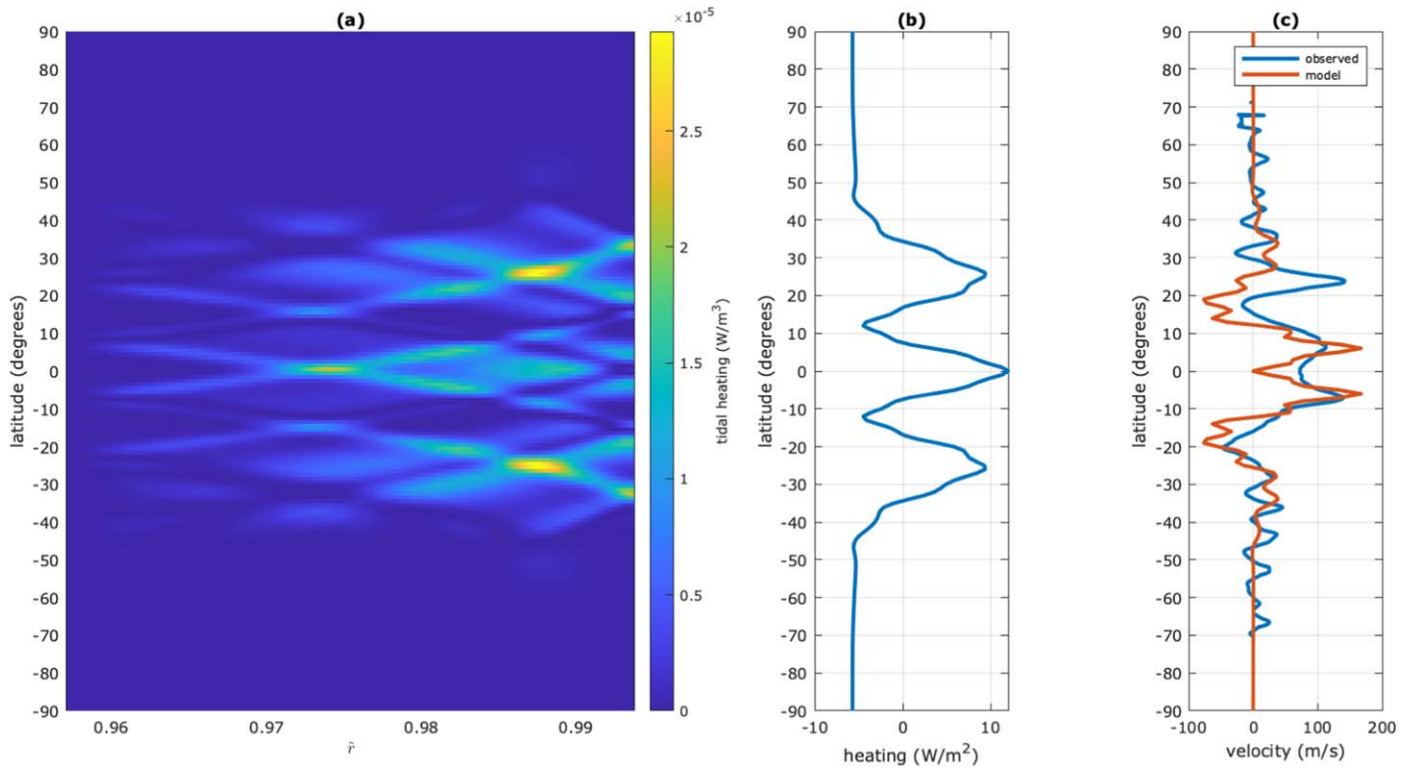


Figure 1. (a) Model of Jupiter’s time-averaged tidal dissipation rate as a function of latitude and nondimensional radius. The dissipation in panel (a) is depth integrated, and the global average is removed to give the three-peak curve in panel (b). This is then regarded as a source/sink of pressure/heating driving geostrophic jets (panel (c)) that show important features in common with the observed jets. Most important in the agreement demonstrated are: the equatorial prograde flow with a local minimum right at the equator, the concentrated activity within the critical latitudes, and the inflection points of band transitions. The most important disagreement seen is the observed asymmetric component of the observations, as this asymmetry is not expected for sectoral tidal forces and spherically symmetric interior parameters.

3. Numerical Results for Jupiter

The details of the TROPF tide model configuration for this study are described in Appendix B. Here the primary results addressing the goals of this study are described.

First, the horizontal and vertical eigenvalues/functions were calculated and found to show broad overlap for $\tilde{\epsilon}_{e,(\mu>2)}^2$, supporting an expectation for resonantly forced modes (see Appendix B.4.) The largest-scale mode that can be resonantly excited involves the third (i.e., second symmetric) horizontal “Hough” eigenfunction. The pressure and flow fields for this mode are similar to “Case B” in Appendix B.5 where one can also see the time-averaged dissipation having three prominent peaks with respect to latitude.

Second, the three-dimensional tidal response was calculated. The matrix version of the governing Equation (1) was solved to obtain the coefficient vector for \tilde{p} , from which the flow and auxiliary variables were obtained as described in Tyler (2019a). An important demonstration is that the time-averaged dissipation rate (Figure 1(a)) shows the expected banding between the critical latitudes, with the number and distribution varying with depth. The banding between critical latitudes and variation with depth is also present for other time-averaged variables. A major component of the response appears to involve the third Hough mode as anticipated in the eigenfunction analyses.

Third, a case is demonstrated for jets driven by time-averaged tidal dissipation. The dissipation shown in Figure 1(a) is regarded here as ultimately converted to heat but not necessarily at the same radial location because of vertical propagation. An attempt is not made here to prescribe the

process by which the leaked tidal pressure is converted to heat (different phase-change and radiative processes likely dominate at different depths). Instead, the bulk effect of the depth average of dissipation/heating at creating pressure and geostrophically balanced jets is considered using a simple model as described in Appendix B.3. The results for the tidally driven jets are shown in Figure 1(c) together with observations obtained from Johnson et al. (2018). The results demonstrate a remarkable match in the patterns of the symmetric component of the jets and prograde equatorial flow. Note that in Figure 1(c), the amplitude of the model depth-averaged jets is adjusted for comparison with the observations of jets at the surface. Precise amplitude agreement is not expected given the uncertainty in how well the observed surface jets represent the depth-averaged jets (or how well the bulk modeling resolves dynamics visible at the surface). But as a basic amplitude check, one may infer that because the model tidal heating is found to be comparable to the observed endogenic value, it is also adequate for driving jets of the observed amplitude. The amplitude comparison then folds into examination of the sensitivity of the model tidal power to the assumed dissipation timescale, as described in Appendix B.2.

4. Conclusions

Below, conclusions regarding Jupiter’s tidal response are first given. This is followed by conclusions regarding the banding and jets driven by the tides.

In previous work and extended here, compelling arguments for the expectation of resonantly forced tidal modes with strong

rotational scattering has been made using theory and by rough estimates of Jupiter's internal parameters. Here, the predicted resonantly forced modes and rotational scattering are also explicitly demonstrated in a three-dimensional tidal model with prescribed Juno-derived interior parameters as input. The conclusion of this study is then that there are high-powered resonantly forced modes in Jupiter's tidal response. This conclusion is expected to be robust because it follows primarily from just the fast rotation and presence stratification, rather than any tight restriction on the associated input parameters. (One can see that the tidal response for a fast-rotating, underdamped, and continuously stratified fluid will have tidal-response modes spanning regions in the lower-right corner of Figure 6 permeated by rotational-gravity resonance peaks.) The fast rotation of Jupiter is clear, but the assumed stratification is contingent on both the assumed density profile and fluid adiabatic index (Γ_1). Here, the density profile assumed comes from an independent study fitting Juno gravity observations. While the density profile obtained from gravity data is not unique, this nonuniqueness is more important for the core and deep interior, while the methodology has better sensitivity in resolving the outer layers. Hence, it is not expected that there will arrive a more realistic density profile that is somehow different enough to change the conclusion of resonant modes. The adiabatic index (assumed here to be $\Gamma_1 = 2$, reflecting a polytropic fluid) is uncertain because it varies with the equation of state of the fluid assumed. Plausible variations in Γ_1 do change the stratification parameters and thereby have a significant effect on the tidal response calculated. But outside of some pathological examples (a choice of $\Gamma_1(\tilde{r})$, which happens to make $N^2(\tilde{r})$ vanish everywhere), it is not expected that a more realistic description of Γ_1 will change the conclusion regarding resonant modes.

The resonant tidal modes have a latitudinal dependence that will drive banded time-mean tidal effects such as the jets in Figure 1(c). How robust is this conclusion? Let us consider it in parts. First, the existence of critical latitudes where there is a wavelike/evanescent transition of dynamical behavior at the location where the forcing frequency happens to match that of rotation is very clearly expected from the governing equations of CTT. The specific result of critical latitudes at $\pm 50^\circ$ then robustly follows from consideration of sectoral tidal forces raised by Io. Second, the expectation that time-mean tidal effects will appear in bands between the critical latitudes is also very robust, as it is a related consequence of the rotational scattering. However, the number of bands and their latitudinal locations and thicknesses are very sensitive to the internal parameters assumed. Assuming, as here, sectoral tidal forces and radially symmetric fluid parameters, the banding should be symmetric about the equator. Observations show asymmetric components in the jets. It does not seem that this negates conclusions here but rather that it reflects the departures in symmetry in the fluid parameters. The asymmetric magnetic field, for example, will lead to asymmetric ohmic drag in the deeper conductive fluid and possibly surface expressions of this. As long demonstrated by the Great Red Spot, Jupiter's interior is clearly not radially symmetric, but it still appears to be a reasonable approximation for starting tidal models.

While banding between the critical latitudes appears to be a robust prediction of the tide model, do the details of the predicted bands match observations? While we use the tidal solution to provide a demonstration of tidal bands and jets in

reasonable agreement with observations, the specific result for the jets should be regarded as somewhat less robust than the result for the banding because additional assumptions are required to calculate the jets from the tidal heat. Specifically, the interesting demonstration that the time-mean of tidal heating will vary with latitude and depth (Figure 1(a)) and appear banded in its depth average (Figure 1(b)) follows directly from the tidal solution, whereas the description of the jets (Figure 1(c)) requires additional model assumptions. Note that the simple geostrophic-balance model used here is clearly chosen for its simplicity, and so it is not the case that we have selected exotic model assumptions in order to match the observed jets. But it is easily possible that other model or process assumptions may produce tidally driven jets also in agreement with the observations. The time-mean tidal effect specifically considered here for driving the jets is dissipative heating, but the banding exists in other time-mean tidal effects as well such as the Eliassen-Palm fluxes considered in Ioannou & Lindzen (1994).

Interestingly, the agreement in the details of the modeled and observed jets easily disappears if one alters significantly the interior parameter assumptions or the dissipation process assumed (e.g., different stratification will produce a different number and spacing of jets, and dissipation parameterized as drag of horizontal momentum gives the wrong parity.) A description of the sensitivity of tidal power to input parameters is compactly shown in Figure 6, whereas several examples showing how the latitudinal band number (and the number of heating peaks) as well as the tidal flow field vary with input assumptions is shown in Figure 7. While the jets calculated are illustrative in this study, after further vetting, it may be reasonable to use such observed time-mean tidal effects to infer or confirm models of interior parameters and processes, as suggested in Lindzen (1991). A preliminary claim could be that the agreements shown here already provide some validation for the Juno-inferred density profile, as the model results depend sensitively on the profile assumed (as well as the adiabatic index). In any case, these tidal results are highly relevant to the interpretation and modeling of Juno data and should be considered.

The author thanks Dongdong Ni for providing the Juno-derived density-profile data and Raul Morales Juberias for providing the data for the observed latitudinal profile of the jets. Parts of this work were supported by NASA (grant numbers NNX15AT34A and 80GSFC21M0002) and NSF (grant number 2048788).

Appendix A

Summary of the TROPF Formulation and Methodology

The Tidal Response Of Planetary Fluids (TROPF) is most essentially a collection of algorithms for efficiently solving problems in classical tidal theory (CTT) using factorized sparse matrices. The TROPF manual describes several different formulations of the governing equation(s), multiple solution methods, validations of the methods, and an extensive description of the generic solutions to the range of typical cases involving tidal forces in synchronous or nonsynchronously rotating binary systems.

TROPF also includes a software package of the solution methods coded in Matlab, but, as can be seen in Table 3, simple instructions are given for immediately coding the factorized

sparse matrices in the language of choice. (The expression for the operator \mathcal{L}_V depends on the fluid considered and is described in detail in Appendix A.1.) TROPF includes both spherical-harmonic and finite-volume routines for solving the nondimensionalized equations of CTT. The finite-volume routines were included and used in Tyler (2019a) for the purpose of cross-validation of results obtained using the spherical-harmonic routines, but these slower routines also increase TROPF versatility by allowing cases involving horizontal variations in fluid parameters. In application to Jupiter, it is assumed that the fluid parameters vary only radially and so the faster spherical-harmonic base method is used.

In the most general form, the governing equations solved in the TROPF (frequency-domain, spherical-harmonic) routines are the horizontal and vertical balance equations

$$[\tilde{\partial}_t + \mathcal{L}_{\tilde{\alpha}} + \tilde{f} \hat{\mathbf{r}} \times] \tilde{\mathbf{u}}_H = -\tilde{\nabla}_H(\tilde{p} - \tilde{\mathfrak{G}}) + \tilde{\mathbf{F}}_H^{(p)}, \quad (\text{A1})$$

$$\tilde{\nabla}_H \cdot \tilde{\mathbf{u}}_H = -\mathcal{L}_V \tilde{\partial}_t \tilde{p} + \tilde{s}, \quad (\text{A2})$$

where the operator $\tilde{\partial}_t$ is treated as an imaginary constant reflecting the frequency of the prescribed forcing ($\tilde{\mathfrak{G}}$, $\tilde{\mathbf{F}}_H^{(p)}$, or \tilde{s}). Note that $\tilde{\mathbf{F}}_H^{(p)}$ and \tilde{s} are absent when considering (as in the tidal component of this study) only the horizontal components of tidal forces due to the prescribed tidal potential $-\tilde{\mathfrak{G}}$.

In the most efficient of the TROPF routines (and used in this study), these equations are combined into a single equation for \tilde{p} . Some insight on how this can be done is easily seen in the case where it is assumed that the dissipation operator $\mathcal{L}_{\tilde{\alpha}}$ can also be treated as a constant (an inverse timescale for drag). In this case, the operator on the left-hand side of Equation (A1) can be analytically inverted

$$\begin{aligned} & [\tilde{\partial}_t + \mathcal{L}_{\tilde{\alpha}} + \tilde{f} \hat{\mathbf{r}} \times]^{-1} \\ & = ((\tilde{\partial}_t + \mathcal{L}_{\tilde{\alpha}})^2 + \tilde{f}^2)^{-1} [\tilde{\partial}_t + \mathcal{L}_{\tilde{\alpha}} - \tilde{f} \hat{\mathbf{r}} \times], \end{aligned} \quad (\text{A3})$$

and applied to obtain the solution for $\tilde{\mathbf{u}}_H$. One can then apply the horizontal divergence and combine with Equation (A2) to remove $\tilde{\nabla}_H \cdot \tilde{\mathbf{u}}_H$.

The method for combining the equations is in fact substantially more involved in TROPF, as it involves first a decomposition of $\tilde{\mathbf{u}}_H$ into rotational and divergent Helmholtz potentials. Aside from distinguishing rotational and divergent flow, the added complication in the formulation has the benefit of allowing for a more versatile prescription of $\mathcal{L}_{\tilde{\alpha}}$. Most importantly for simplified coding and computational efficiency, when using a spherical-harmonic base, the governing operators can be represented through matrix multiplication of very basic sparse (diagonal, bi-diagonal, and tri-diagonal) suboperator matrices.

As described in detail in Tyler (2019a), Equations (A1) and (A2) are combined to give

$$\mathcal{L}_{\tilde{p}}\{\tilde{p}\} = i\tilde{\mathfrak{G}} + \tilde{Q}_{\tilde{p}}, \quad (\text{A4})$$

where

$$\begin{aligned} \tilde{Q}_{\tilde{p}} = & -[\mathcal{L}_L^{-1}[\mathcal{L}_A - \mathcal{L}_C \mathcal{L}_B^{-1} \mathcal{L}_C] \mathcal{L}_L^{-1}] \tilde{s} + \mathcal{L}_L^{-1} \{ \tilde{\nabla}_H \cdot (i \tilde{\mathbf{F}}_H^{(p)}) \} \\ & + [\mathcal{L}_L^{-1} \mathcal{L}_C \mathcal{L}_B^{-1}] \{ \tilde{\nabla} \cdot (\hat{\mathbf{r}} \times \tilde{\mathbf{F}}_H^{(p)}) \}, \end{aligned} \quad (\text{A5})$$

is absent in the tidal forcing case.

In the spherical-harmonic TROPF solution routines, the operators \mathcal{L} are replaced with square matrix operators L , and the solution variables are replaced with a vector for the spherical-harmonic coefficients. Note that the governing operator tri-diagonal matrix, L_H is constructed from simply defined suboperator matrices, all of which are diagonal except for L_C , which is a sparse bi-diagonal. Because the formulation avoids needing L_C^{-1} , the only suboperators that need explicit inverse forms are diagonal, and these inversions are prescribed analytically. Hence, the TROPF formulation is very efficient in maintaining extremely sparse matrices, and numerical steps have been replaced with analytical ones where possible.

The description in Tyler (2019a) treats the vertical operator matrix L_V as a constant or diagonal matrix (as appropriate for barotropic fluids or for a baroclinic mode). Here, we represent L_V as a differential operator (see Appendix A.1) discretized with finite-differences. To allow this, we first create a sparse supermatrix with N_r block diagonals (each N by N) representing the horizontal operations, then add the elements for L_V , and then adjust the matrix for boundary conditions. N_r is the number of radial points, and N is the number of spherical harmonics in the expansion. In the calculations in this study, there are $N = 150$ spherical harmonics at each of $N = 1835$ equally spaced radial layers. Each of the operator and suboperator matrices are then of size 275,250 by 275,250, which would make storage and computations unfeasible if any of the matrices were not sparse (as would be the case if the traditional Laplace tidal operator L_H^{-1} were required).

In the TROPF manual and applications, a description of how to improve accuracy with various corrections (e.g., self-gravity, nonlinearity, scale-dependent dissipation, and dispersion) is included. One could also relax the traditional approximation through iteration. It is not expected that results with these additional effects would change the types of comparisons required in this study, and therefore to simplify interpretation of results, they are not included. In other studies (e.g., precise comparison of tidally generated mass anomalies with gravity data), the corrections (e.g., self-gravity) could be crucial.

A.1. Vertical Operator \mathcal{L}_V

The derivation of the vertical operator is described in Tyler (2019a, 2019b). For a variety of fluids, it can be represented as

$$\mathcal{L}_V\{\cdot\} = [[\mathcal{Y}_1][\chi_1 + \tilde{\partial}_r][\mathcal{Y}_2][\chi_2 + \tilde{\partial}_r] + \mathcal{Y}_3]\{\cdot\}, \quad (\text{A6})$$

where the radially dependent parameters \mathcal{Y}_1 , \mathcal{Y}_2 , \mathcal{Y}_3 , χ_1 , and χ_2 depend on the fluid considered.

Isolating terms of differential order, Equation (A6) can also be written as

$$\mathcal{L}_V\{\cdot\} = [A_2 \tilde{\partial}_r \tilde{\partial}_r + A_1 \tilde{\partial}_r + A_0]\{\cdot\}, \quad (\text{A7})$$

where $A_2 = \mathcal{Y}_1 \mathcal{Y}_2$, $A_1 = \mathcal{Y}_1 \tilde{\partial}_r \{\mathcal{Y}_2\} + \mathcal{Y}_1 \mathcal{Y}_2 (\chi_1 + \chi_2)$, $A_0 = \mathcal{Y}_1 \tilde{\partial}_r \{\mathcal{Y}_2 \chi_2\} + \mathcal{Y}_1 \mathcal{Y}_2 \chi_1 \chi_2 + \mathcal{Y}_3$.

The formulation in Equations (A6) and (A7) involves the nondimensional operator $\tilde{\partial}_r = \tilde{r} \partial_{\tilde{r}} (= r \partial_r)$ and thereby differential operations with respect to $\ln \tilde{r}$. Rewritten in terms of the conventional $\partial_{\tilde{r}}$, Equations (A6) and (A7) can be written as

$$\mathcal{L}_V\{\cdot\} = [[\mathcal{Y}_1][\chi_1 + \tilde{r} \partial_{\tilde{r}}][\mathcal{Y}_2][\chi_2 + \tilde{r} \partial_{\tilde{r}}] + \mathcal{Y}_3]\{\cdot\}, \quad (\text{A8})$$

$$\mathcal{L}_V\{\cdot\} = [B_2 \partial_{\tilde{r}} \partial_{\tilde{r}} + B_1 \partial_{\tilde{r}} + B_0]\{\cdot\}, \quad (\text{A9})$$

where $B_2 = \mathcal{Y}_1 \mathcal{Y}_2 \tilde{r}^2$, $B_1 = \tilde{r}^2 \mathcal{Y}_1 \partial_{\tilde{r}} \{\mathcal{Y}_2\} + \tilde{r} \mathcal{Y}_1 \mathcal{Y}_2 (1 + \chi_1 + \chi_2)$, $B_0 = \mathcal{Y}_1 \tilde{r} \partial_{\tilde{r}} \{\mathcal{Y}_2 \chi_2\} + \mathcal{Y}_1 \mathcal{Y}_2 \chi_1 \chi_2 + \mathcal{Y}_3$.

Note that while the operator $\tilde{\partial}_r$ has eigenfunctions of the form \tilde{r}^q (where q is a constant), the more conventional operator $\partial_{\tilde{r}}$ has eigenfunctions of the form $e^{-k\tilde{r}}$ (where k is a constant). In tidal studies, an advantage of choosing the operator $\tilde{\partial}_r$ comes in anticipating the form of the tidal forces. The tidal forces are usually expressed as terms from a spherical-harmonic expansion of the time-varying gravitational potential ($-\tilde{\Phi}$) where the radial dependence is \tilde{r}^{q_F} , with q_F a constant (integer). (Laplace created the spherical-harmonic expansion in the context of this application.) Hence, the forcing terms are already expressed as eigenfunctions of the operator $\tilde{\partial}_r$. This was exploited in Tyler (2019b) to provide an analytical description of the particular solution to the governing equations under the assumption of constant (or slowly varying) coefficients A_2 , A_1 , and A_0 . (See Appendix C for the details of this analytical approach to solutions.)

A.1.1. \mathcal{L}_V Parameters for a Stratified, Nonhydrostatic, Compressible Fluid (Jupiter)

In the simplest case of a uniform-density fluid or a single baroclinic mode, Υ_1 , Υ_2 , χ_1 , and χ_2 vanish, and $\Upsilon_3 = \tilde{v}^2$, where \tilde{v} is the slowness parameter (Tyler 2019a). While \tilde{v}^2 can include an imaginary part representing attenuation in the vertical dynamics and/or dependence on spherical-harmonic degree (dispersion), the name comes from the fact that the real component of \tilde{v} describes an inverse wave speed. In a barotropic (or equivalent barotropic) thin fluid with dissipation only through \mathcal{L}_H , \tilde{v} is simply the inverse of the shallow-water wave speed (perhaps calculated with a reduced gravity or equivalent depth).

For the case of a stratified, nonhydrostatic, compressible atmosphere on Jupiter, the case is more complicated. As in Tyler (2019b), the equations assumed in this study to describe the vertical structure are those in Ioannou & Lindzen (1993b) but modified to include a heat source and Newtonian cooling as in Auclair-Desrotour et al. (2016), and a generic pressure relaxation (with time constant $\tilde{\alpha}_p$) as in Tyler (2019a). In this case, $\Upsilon_1 = -\tilde{r}$, $\Upsilon_2 = (\tilde{r}(\tilde{\partial}_t\tilde{\partial}_t + \gamma_p\tilde{N}^2))^{-1}$, $\Upsilon_3 = \frac{\gamma_p}{\gamma_t}\frac{1}{\tilde{c}_s^2}$, $\chi_1 = -\frac{\tilde{g}_0}{\tilde{c}_s^2} + (\gamma_p - 1)\frac{\tilde{N}^2}{\tilde{g}_0} + 2$, $\chi_2 = \frac{\tilde{g}_0}{\tilde{c}_s^2}\left(\frac{\gamma_p}{\gamma_t} - 1\right) - \frac{\tilde{N}^2}{\tilde{g}_0}$. The parameters γ_p , γ_t are each unity unless Newtonian cooling is included, in which case $\gamma_p = (1 + \sigma_0/\partial_t)^{-1}$, $\gamma_t = (1 + \Gamma_1\sigma_0/\partial_t)^{-1}$, where σ_0 is the attenuation frequency described in Auclair-Desrotour et al. (2016). For the thick Jovian atmosphere, the Newtonian cooling is not an appropriate model, and an appropriate model of even the dominant physical process is not known. Instead, we represent vertical attenuation more simply by adding a pressure relaxation term with coefficient $\tilde{\alpha}_p$ as in Tyler (2019a). This amounts to calculating \mathcal{L}_V (with $\gamma_t = \gamma_p = 1$) and then modifying as $\mathcal{L}_V \rightarrow (1 + \tilde{\alpha}_p/\partial_t)\mathcal{L}_V$ to add a small imaginary part representing the relaxation of pressure due to unresolved processes in the vertical balance. While Newtonian cooling also amounts to including an imaginary component of \mathcal{L}_V , the model chosen here does not suggest or require a similar process of radiative cooling.

To allow for forcing by nonzero $\tilde{\partial}_r\tilde{\Phi}$ and heat sources $\tilde{\mathcal{J}}$, we must simultaneously choose

$$\tilde{s} = [\Upsilon_1][\chi_1 + \tilde{\partial}_r][\Upsilon_2]\left\{\tilde{\partial}_r\{\tilde{\partial}_t\tilde{\Phi}\} + \tilde{g}_0\frac{\gamma_p\Gamma_1\kappa\tilde{\mathcal{J}}}{\tilde{c}_s^2}\right\} + \frac{\gamma_p\Gamma_1\kappa\tilde{\mathcal{J}}}{\tilde{c}_s^2}, \quad (\text{A10})$$

(see Tyler 2019a, 2019b), and this closes the coupled set of Equations (A1) and (A2).

Because the vertical velocity is often used in the boundary conditions, it is helpful to explicitly describe here its relationship to the solution variable \tilde{p} :

$$\tilde{w} = \tilde{r}\tilde{\Upsilon}_2\left(-[\chi_2 + \tilde{\partial}_r]\tilde{\partial}_t\tilde{p} + \tilde{\partial}_r\tilde{\partial}_t\tilde{\Phi} + \gamma_p\frac{\tilde{g}_0\Gamma_1\kappa\tilde{\mathcal{J}}}{\tilde{c}_s^2}\right). \quad (\text{A11})$$

Appendix B Application to Jupiter

B.1. Calculation of Internal Parameters

The density-profile data obtained from the Juno gravity data of Ni (2018), shown in Figure 2(a), was interpolated onto the radial grid of this study to provide the background density ρ_0 as a function of fractional radius (\tilde{r}). The background pressure p_0 (Figure 2(b)) was obtained following the hydrostatic relationship with rotational correction as in Ni (2018). In this study, only data in the outer shell (Figures 2(c), (d)) are used.

The gravitational acceleration g (Figure 3(a)) is calculated as the gradient of the gravitational potential obtained from a running integral of the density in Figure 2(c). As in Auclair-Desrotour et al. (2016), the speed of sound c_s (Figure 3(c)) is defined as $(\Gamma_1 p_0/\rho_0)^{1/2}$, and the buoyancy frequency (Figure 3(e)) for the compressible media is $N = (-g(\partial_r \ln \rho_0 - \Gamma_1^{-1}\partial_r \ln p_0))^{1/2}$. The nondimensional versions of these parameters (using the scaling factors described in Table 1) are shown in Figures 2(b), (d), and (f). While the appropriate adiabatic index Γ_1 is uncertain, here the value $\Gamma_1 = 2$ is used following the description for a polytropic interior in Ioannou & Lindzen (1993a, 1993b; French et al. 2012). The model does not extend into the atmosphere above the 100 bar layer where the adiabatic index should shift toward that of a perfect gas (1.4) or other assumption. While there is very little mass in this missing upper region for the tidal forces to work on, including it in the model could be important in a future study aimed at including a more complex and realistic radial variation in the assumed equation of state and dissipation process.

The model easily allows an arbitrary prescription of $\Gamma_1(\tilde{r})$ as well as the prescription of more complex/realistic dissipation schemes. Similarly, TROPF already includes routines for including self-gravity. The goals of this study are, however, to provide an initial demonstration of key tidal effects using the simplest prescribed model. Future studies extending from here will need to include study of the sensitivity of results to the uncertainties in these model prescriptions, and so the simple model in this study also provides a useful baseline and starting point.

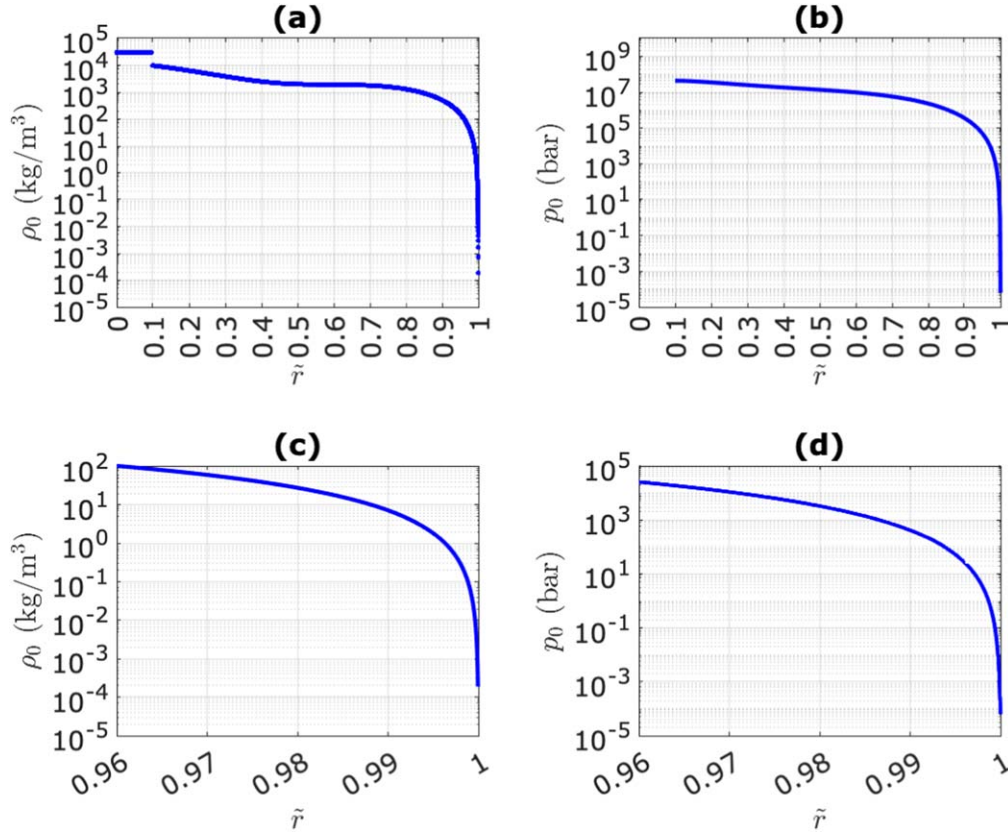


Figure 2. Background density ρ_0 (panel (a)), and pressure p_0 (panel (b)). The data in the outer shell (panels (c) and (d)) is used in this study.

B.2. Calculation of Tides

The tides are calculated using TROPF as described in Appendix A. The vertical operator \mathcal{L}_V is calculated as described in Appendix A.1.1 using the internal parameters described in Appendix B.1. The only dissipation included is the pressure relaxation term described in Appendix A.1.1. The spherical-harmonic expansions are truncated to 150 terms, and 1835 equally spaced radial grid points span the 3000 km shell. All other parameters for the forcing and response follow those of the previous study in Tyler (2019b).

More specifically, in this study, the dissipation parameter $\tilde{\alpha}_p$ is chosen to be linearly proportional to \mathcal{L}_V^{-1} (implying more attenuation for faster wave modes) such that inclusion of dissipation is obtained by the simple transformation $\mathcal{L}_V \rightarrow \mathcal{L}_V + (\tilde{\beta}_p / \tilde{\partial}_t)$, where $\tilde{\beta}_p$ is a prescribed constant. While, $\tilde{\beta}_p$ is regarded as arbitrary because a physical dissipation model is not proposed, a constraint is that the tidal power not exceed the observed endogenic value, and that the value seems reasonable with other checks. Here, $\tilde{\beta}_p = 2 \times 10^{-4} / (2\Omega)$ is chosen because it provides power reaching but not exceeding the endogenic value. Higher values for $\tilde{\beta}_p$ produce tidal power that is too high. So an appropriately prescribed $\tilde{\beta}_p$ cannot be higher. Could it be much lower? Yes, the tidal banding does not require that the tides produce heating rates comparable to the observed endogenic values. Perhaps a minimum $\tilde{\beta}_p$ constraint can be formulated by considering the power required to drive the jets, but that is not pursued in this study, which follows the simplified model assumptions. As an additional check, one can, however, consider the implied dissipation timescale $\tilde{\alpha}_p^{-1} = \tilde{\beta}_p^{-1} \mathcal{L}_V \approx \tilde{\beta}_p^{-1} \tilde{\nu}_{(\lambda)}^2$. In dimensional units, the implied

dissipation timescales are 4.6, 13, 32, 64, and 109 days for the first five vertical eigenmodes. For comparison, in application to thick atmospheres (Venus), Auclair-Desrotour et al. (2016) described an appropriate value for the dissipation timescale associated with Newtonian cooling to be 15 days.

B.3. Calculation of Jets

Time-mean pressure \bar{p} is estimated from the depth average of time-mean tidal heating \mathfrak{J} as follows. The linearized thermodynamic equation (one of the underlying equations of \mathcal{L}_V in this study, see Appendix A.1, and described in Auclair-Desrotour et al. 2016) for steady state and assuming that vertical velocity vanishes becomes $\bar{p} / \rho_0 = \alpha_t^{-1} (\Gamma_1 - 1) \mathfrak{J}$, where α_t^{-1} is a thermal radiation timescale originally formulated for Newtonian cooling. Using this together with the dimensionalized version of Equation (A1), with \mathfrak{G} and $\mathbf{F}_H^{(p)}$ absent, and applying the operator in Equation (A3) for steady state and with dissipation represented by a simple drag coefficient α , the time-mean velocity $\bar{\mathbf{u}}_H$ is obtained as

$$\bar{\mathbf{u}}_H = -\rho_0^{-1} (\alpha^2 + f^2)^{-1} [\alpha - f \hat{\mathbf{r}} \times] \nabla_H \bar{p}. \quad (\text{B1})$$

The flow is approximately in geostrophic balance. A small drag coefficient $\alpha = 5 \times 10^{-2} (2\Omega)$ is included to stabilize the flow near the equator where f vanishes. The model jets calculated in this study have been described as arbitrarily rescaled for comparison with observations, but one can show that the required scaling would be accomplished with the assumption $\alpha_t = 1.2 \times 10^{-4}$ (1/s). Of course, the modeled jets calculated here reflect average/bulk flow and, the amplitude need not match that of the jets observed at the surface.

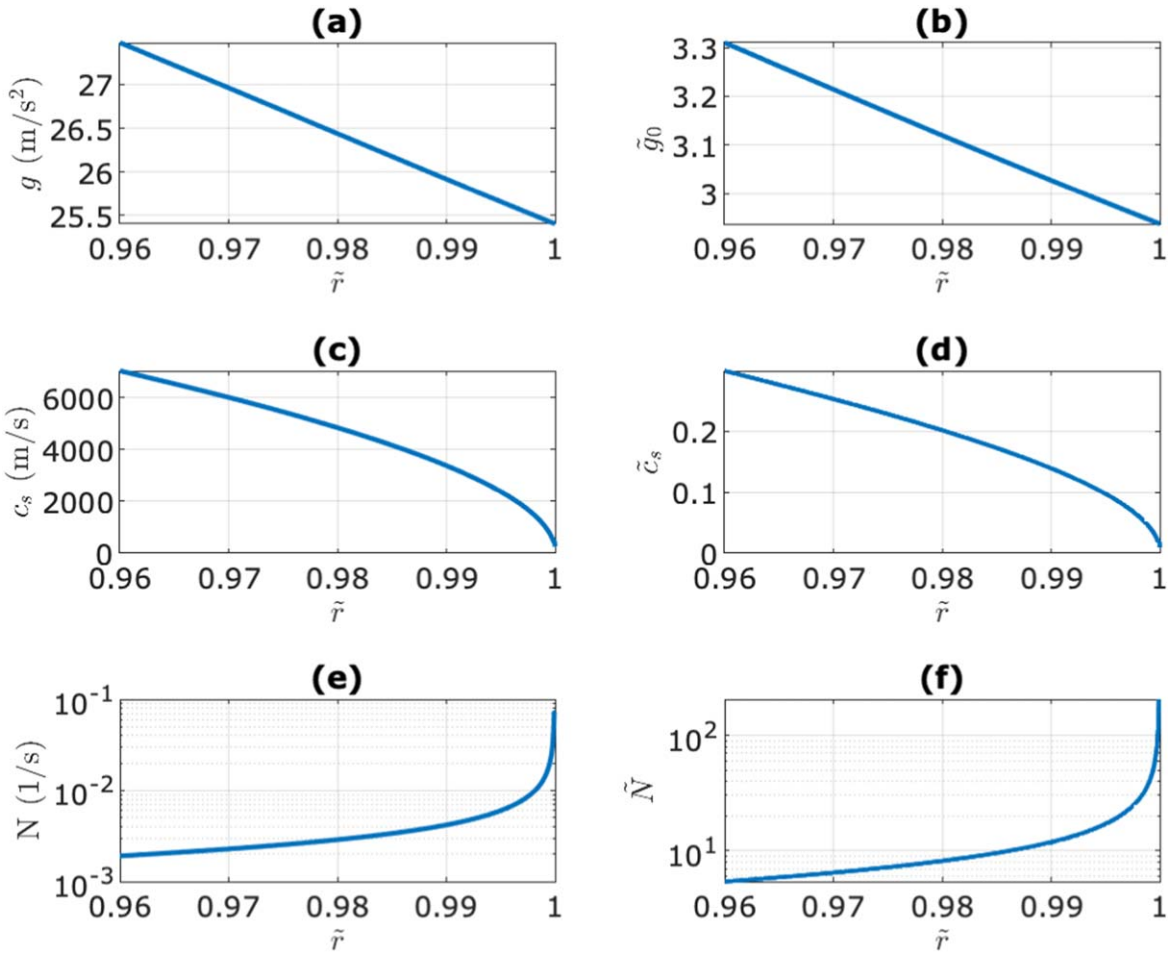


Figure 3. The gravitational acceleration g (panel (a)) speed of sound \tilde{c}_s (panel (c)) and buoyancy frequency N (panel (e)) and their nondimensional forms (panels (b), (d), and (f)).

B.4. Eigenvalues and Eigenfunctions of \mathcal{L}_H and \mathcal{L}_V

The eigenvalues and eigenfunctions of \mathcal{L}_H and \mathcal{L}_V are calculated from their matrix operators L_H and L_V and presented in Figures 4 and 5. The eigenfunctions of L_H describe the coefficient for the spherical harmonics components. The eigenfunctions of L_V describe the amplitudes at the radial grid points in the finite-difference base.

As shown by the spherical-harmonic coefficients, the largest (positive) eigenvalues $\tilde{c}_{e,(\mu)}^2$ are associated with the largest-scale horizontal spatial modes. The largest $\tilde{\nu}_{(\lambda)}^{-2}$ are associated with the longest vertical wavelengths. The first vertical mode depends sensitively on the boundary condition assumptions. In the case here, its eigenvalue is negative and does not closely overlap any of those for the horizontal structure. While overlap begins broadly for the higher eigenmodes, only the symmetric horizontal eigenmodes (having odd eigenmode number) will be excited by sectoral tidal forces. Hence, the largest spatial mode for which overlap and resonant excitation is expected to begin is for $\mu = 3$.

B.5. Interpretation of Dominant Modes in the Tidal Response

The tidal solution provides both the spherical-harmonic coefficients and three-dimensional fields for the primary and

auxiliary solution variables. To understand the modes involved in the response, it is helpful to review the approach in Tyler (2019b).

As described in Appendix C.2, one may consider tidal solutions for a prescribed vertical mode whereby \mathcal{L}_V is prescribed to be the squared slowness $\tilde{\nu}^2$ associated with that mode. The real part of $\tilde{\nu}^{-2}$ is relabeled as the squared wave speed \tilde{c}_e^2 , and the imaginary part provides the parameter $\tilde{\alpha}_p$, which is translated as the associated dissipation timescale \tilde{T} . Because TROPF is fast, millions of high-resolution tidal scenarios can be calculated in minutes to fully sample the solution domain and provide a description of tidal power as a function of the input parameters \tilde{c}_e^2, \tilde{T} .

An example of this is shown in Figure 6. Where \tilde{c}_e^2 (dependent on the fluid parameters and vertical structure) is close to one of the eigenvalues $\tilde{c}_{e,(\mu)}^2$ (dependent on the horizontal operator), there can be resonant amplification. From top down, the strong peaks seen in the underdamped region of the solution domain correspond with excitation of the symmetric ($\mu = 1, 3, 5, \dots$) Hough eigenmodes, which can be classified as resonantly forced rotational-gravity waves. Cases A, B, and C show the coordinates of input parameters used for the solutions shown in Figure 7.

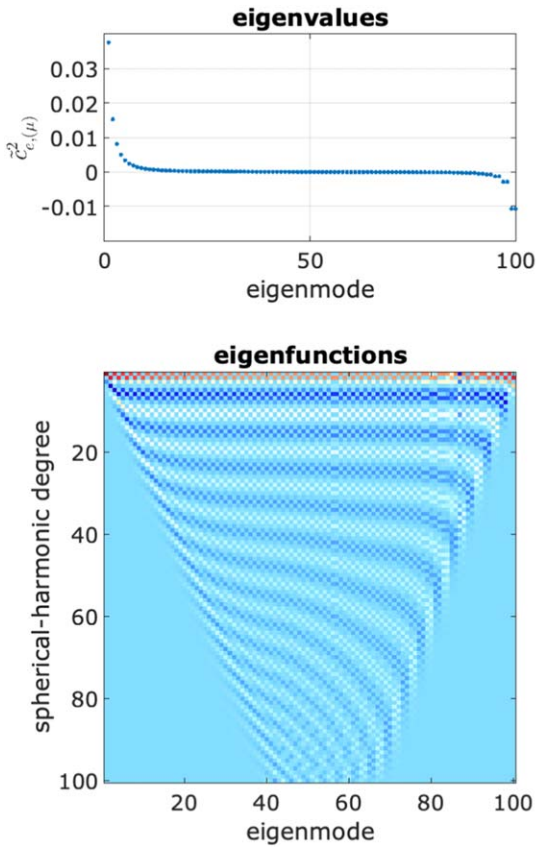


Figure 4. Eigenvalues ($\tilde{c}_{e,\mu}^2$) and eigenfunctions of the horizontal operator L_H . The amplitudes of the spherical-harmonic coefficients show important scattering across higher degrees as the amplitude of the eigenvalue $\tilde{c}_{e,\mu}^2$ decreases.

The nondimensional field \tilde{p} would have unit amplitude in the case of an equilibrium tide. As shown in Figure 7, the amplitude can be much larger due to the resonant amplification. Considering that dissipation increases with at least the square of \tilde{p} , this demonstrates that tidal power can be elevated by many orders of magnitude in resonant conditions. The scattering of the tidal response by rotation is also clearly seen in \tilde{p} , as only Case A shows even a dominance in the degree-two component matching that of the forcing. The flow vectors

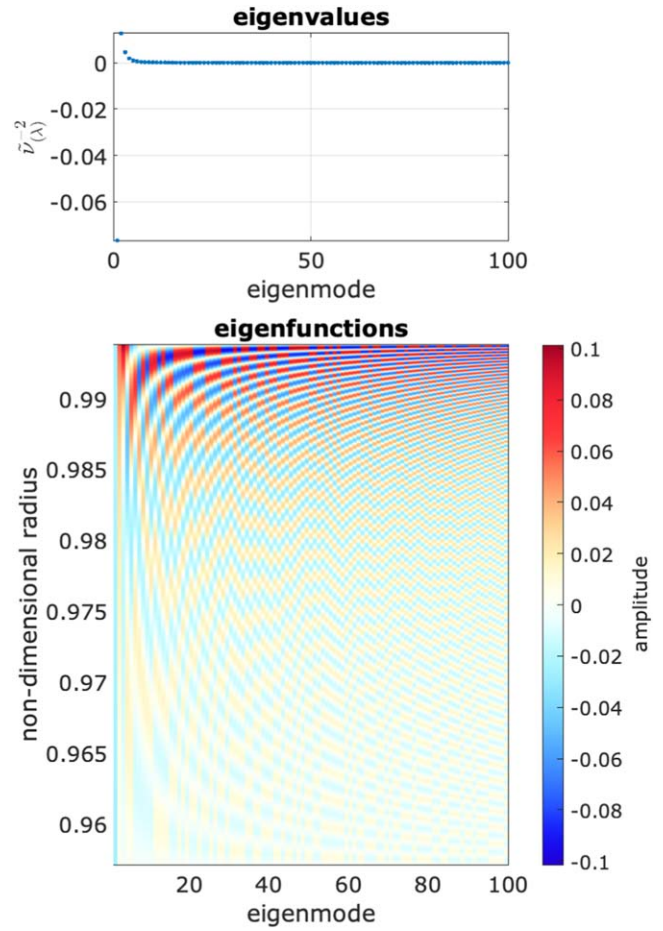


Figure 5. Eigenvalues (plotted as the reciprocal \tilde{v}_{λ}^{-2}) and eigenfunctions of the vertical operator L_V . The eigenfunctions show shorter wavelengths and more focus near the surface for increasing eigenmode.

also show that rotation is important (the flow vectors for the equilibrium tide are quite different).

The bulk dissipation in the tidal model shows predominantly three peaks, suggesting that the $\mu = 3$ eigenmode is an important large-scale contributor. This was also predicted in the analyses in Appendix B.4. Independently, the $\mu = 3$ Case B in the figure also provides jets in the best agreement with those observed. (Note that model jet amplitudes are rescaled for comparison.)

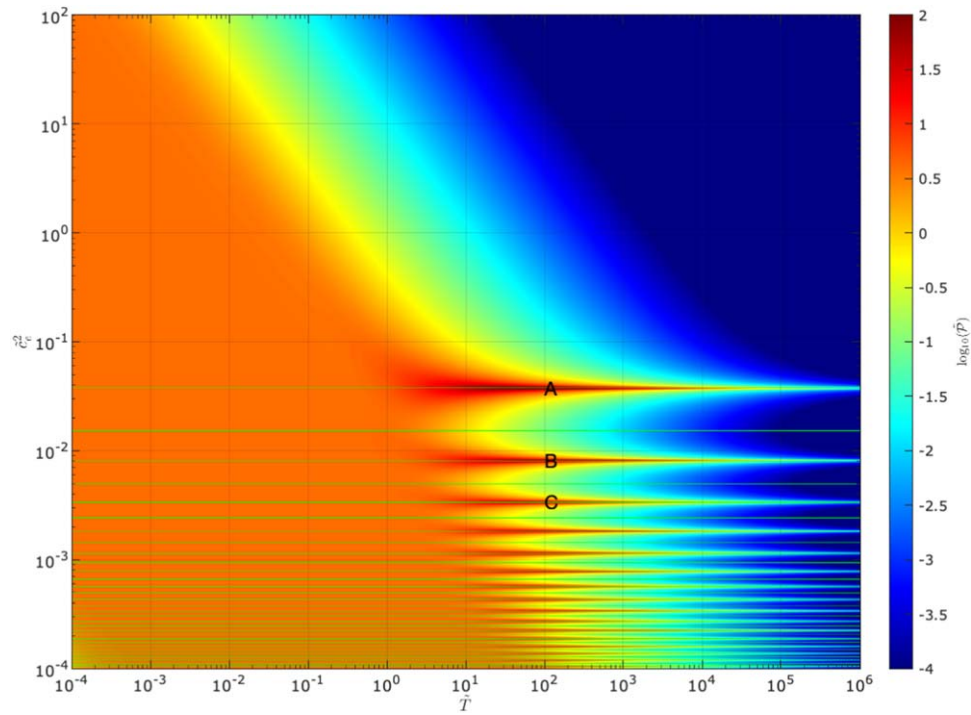


Figure 6. Nondimensional tidal power $\tilde{\mathcal{P}}$ as a function of the squared adjustment wave speed \tilde{c}_e^2 , and the dissipation timescale \tilde{T} (associated with pressure relaxation timescale α_p^{-1}). In the underdamped domain ($\tilde{T} > 1$), three cases (A, B, and C) are considered, corresponding with excitation of the first three symmetric eigen (Hough) functions, respectively. Overlain are horizontal green lines showing the locations of eigenvalues $\tilde{c}_{e,(\mu)}^2$.

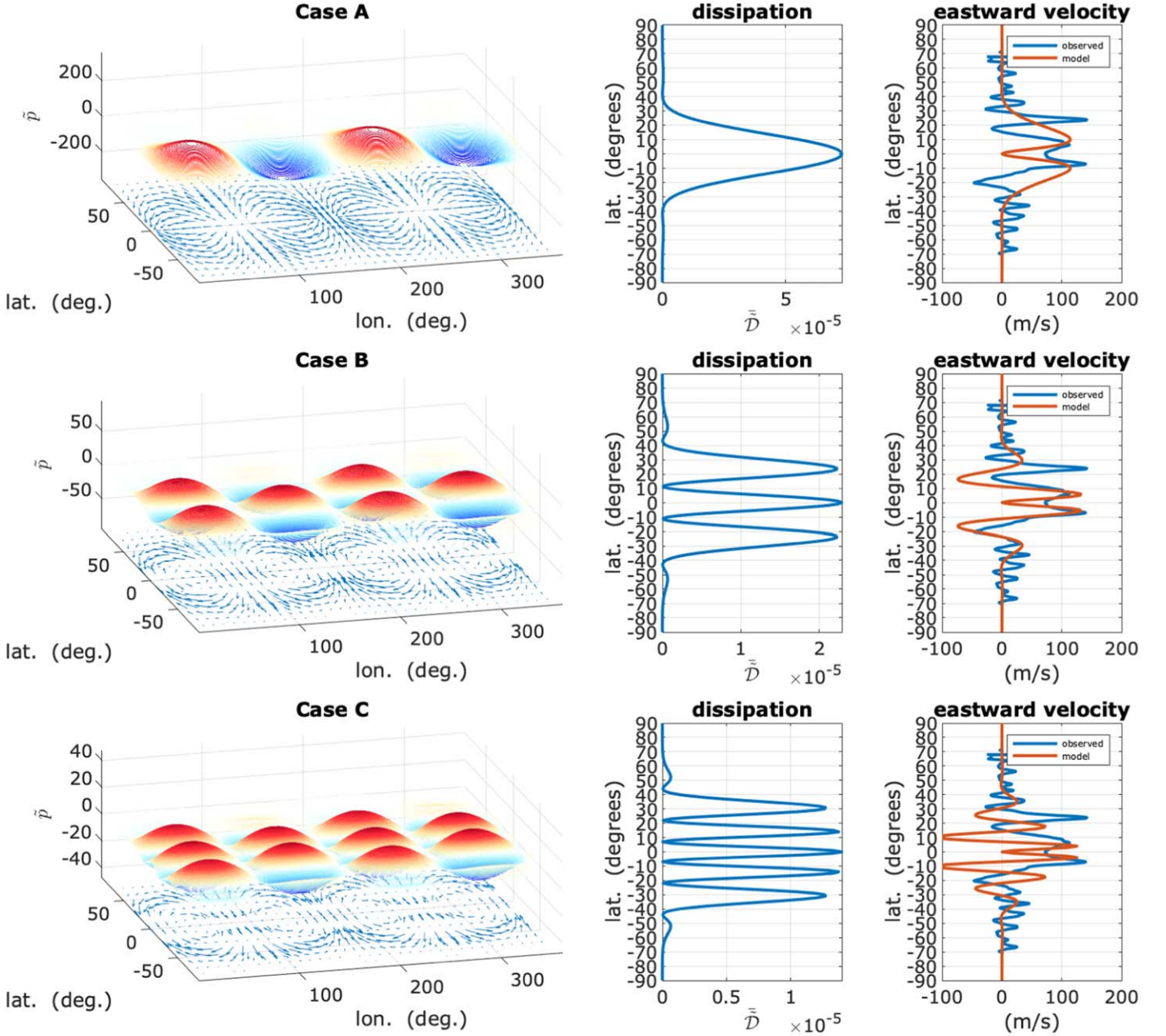


Figure 7. Using the coordinates of Cases A, B, and C in Figure 6, the tidal solutions are recalculated. For each case, the nondimensional reduced pressure \bar{p} is shown in the left panel. The time-averaged dissipation (middle) shows a number of peaks that correspond with the eigenmode number μ . Regarding the dissipation as a pressure/heat source, an illustration of associated geostrophically balanced jets is shown (right) together with the observed profile of the jets.

Appendix C Analytical Solutions

In this section, several methods for obtaining analytical solutions to the tidal response are described. While the tidal solutions presented in this paper rely on the numerical solutions from TROPF, the analytical methods below are useful for gaining intuition and for calculating idealized cases. The methods are particularly useful for understanding which eigenmodes will propagate vertically versus which are evanescent. For example, applying these methods (using the same interior parameters as in the numerical solution described in the main text) to find the local slowness parameter with respect to depth, it was found that the first Hough eigenmode (with the largest spatial scale) is trapped throughout the shell

thickness. Moving through the higher (even) modes, they become trapped only in an increasingly thin layer at the top of the shell. Another important result found using the analytical methods together with Jupiter's interior parameters was that the assumption of slowly varying coefficients was not a good approximation (even for the reformulations of the equations considered) for the shell, especially near the surface.

C.1. Method Using Neumann Expansion of Operator

Under the assumption $\|\mathcal{L}_H \mathcal{L}_V\| < 1$, a Neumann expansion allows the solution of Equation (2) to be written as

$$\bar{p} = [1 - \mathcal{L}_H \mathcal{L}_V]^{-1} \tilde{\Theta} = \sum_{j=0}^{\infty} [\mathcal{L}_H \mathcal{L}_V]^j \tilde{\Theta}, \quad (\text{C1})$$

which involves not integration but simply the repeated application of the analytically prescribed differential operator $\mathcal{L}_T \mathcal{L}_V$ to the prescribed forcing potential $\tilde{\Theta}$. We see that retaining only the $j=0$ term in the series is equivalent to the equilibrium-tide approximation. The additional terms can be regarded as the dynamic departure from that equilibrium. The power, flow, and other tidal variables can then be obtained from the solution \tilde{p} .

This solution, or even consideration of just the first few $j > 0$ additional terms, is very helpful in describing the new physical effects determining the tidal state as it moves from the equilibrium-tide case. These effects include not only the control of wave speed in the adjustment but also the scattering by rotation of energy to other spatial scales. Indeed, the form of the series appears to describe this cascade of energy through sequential spatial scales. The bi-diagonal suboperator L_C describes the scattering of energy to adjacent spherical harmonics (i.e., neighboring spatial scales). Repeated application of L_C (or L_H) suggests the cascade of energy from the degree expressed in the forcing to other degrees expressed in the response.

One can propose a similar Neumann series solution for the case $\|\mathcal{L}_H \mathcal{L}_V\| > 1$. Taking the operations $-\mathcal{L}_H^{-1} \mathcal{L}_H^{-1}$ on Equation (2),

$$[1 - \mathcal{L}_V^{-1} \mathcal{L}_H^{-1}]\{\tilde{p}\} = -\mathcal{L}_V^{-1} \mathcal{L}_H^{-1} \tilde{\Theta}, \quad (\text{C2})$$

and the series solution is

$$\tilde{p} = -[1 - \mathcal{L}_V^{-1} \mathcal{L}_H^{-1}]^{-1} \mathcal{L}_V^{-1} \mathcal{L}_H^{-1} \tilde{\Theta} = -\sum_{j=1}^{\infty} [\mathcal{L}_V^{-1} \mathcal{L}_H^{-1}]^j \tilde{\Theta}. \quad (\text{C3})$$

Note that this solution involves \mathcal{L}_H^{-1} , which can be expressed analytically only when the dissipation operators reduce to simple forms, and even in this less general case, there does not appear to be a simple analytical expression for the associated spherical-harmonic matrix operator L_H . One can in at least the less general case gain insight from this solution to understand the first dynamic departures from an assumed state where the adjustment wave speeds are so small that there is not time during the tidal cycle for the flow to generate a pressure field with a significant back effect on the flow. The solution retaining only the first ($j = 1$) term, for example, describes the pressure field that would be generated by flow responding only to the forcing and not \tilde{p} . The subsequent terms describe this back effect on the flow of the dynamic pressure that develops.

Other approximate analytical solutions to the equations are possible where there is either a large disparity between rotation and forcing frequency amplitudes or when the dissipation timescale is much shorter than either. As these approximations are not expected to be valid for Jupiter's atmosphere, these other forms will not be described here.

The simple analytical solutions can provide very accurate solutions as well as estimates of the errors involved in truncating the series. One may also easily check solutions to verify that the criterion $\|\mathcal{L}_H \mathcal{L}_V\| < 1$ (or $\|\mathcal{L}_V^{-1} \mathcal{L}_H^{-1}\| > 1$) is indeed valid. Hence, these analytical solution could be an easy approach for a variety of tidal studies of Jupiter. This study is specifically aimed at including the description of even the most resonant tidal states where the series solutions are either not

compact or diverge. Therefore, the more general solution method is followed using TROPF.

C.2. Method Using (Vertical or Horizontal) Eigenmode Expansion

In this approach, one considers an eigenmode of either \mathcal{L}_H or \mathcal{L}_V and solves the resulting ordinary differential equation that the governing equation becomes. (In cases where the equations do not remain separable, one could consider instead eigenmodes of the combined operator $\mathcal{L}_H \mathcal{L}_V$.)

Considering the μ th horizontal eigenmode, for example, Equation (2) becomes

$$[1 - \tilde{c}_{e,(\mu)}^2 \mathcal{L}_V]\{\tilde{p}_{(\mu)}\} = \tilde{\Theta}_{(\mu)}. \quad (\text{C4})$$

Substituting using Equation (A7), this becomes

$$-\tilde{c}_{e,(\mu)}^2 [A_2 \tilde{\partial}_r \tilde{\partial}_r + A_1 \tilde{\partial}_r + A_0 - \tilde{c}_{e,(\mu)}^2]\{\tilde{p}_{(\mu)}\} = \tilde{\Theta}_{(\mu)}. \quad (\text{C5})$$

If the coefficients A_2 , A_1 , and A_0 are assumed constant, the particular solution can be immediately obtained from this form of the equation because the tidal potential $\tilde{\Theta}_{(\mu)}$ has the radial dependence \tilde{r}^{q_F} (where q_F is a constant, typically 2) which is an eigenfunction of the operator $\tilde{\partial}_r$. Hence, using $\tilde{\partial}_r \rightarrow q_F$ in Equation (C5), the particular solution is

$$\tilde{p}_{F,(\mu)} = (1 - \tilde{c}_{e,(\mu)}^2 \tilde{\nu}_F^2)^{-1} \tilde{\Theta}_{(\mu)}, \quad (\text{C6})$$

where $\tilde{\nu}_F^2 = A_2 q_F^2 + A_1 q_F + A_0$ is the squared slowness of the particular/forced mode.

The two homogeneous solutions to Equation (C5), \tilde{p}_{h1} , \tilde{p}_{h2} , that may be needed additionally to meet boundary/matching conditions have the form $\tilde{p}_{h,(\mu)} = \tilde{p}_{h\mp,(\mu)} \tilde{r}^{q_h}$, where

$$q_{h,(\mu)} = -\frac{1}{2} \frac{A_1}{A_2} \left(1 \mp \left(1 - 4 \frac{A_2}{A_1^2} (A_0 - \tilde{c}_{e,(\mu)}^2) \right)^{1/2} \right), \quad (\text{C7})$$

and $\tilde{p}_{h\mp,(\mu)}$ is a constant varying with the sign choice.

Combining the particular and homogeneous solutions and summing over the eigencomponents, the full solution $\tilde{p} = \tilde{p}_F + \tilde{p}_{h1} + \tilde{p}_{h2}$ can be written as

$$\tilde{p} = \sum_{\mu} \tilde{p}_{(\mu)} = \sum_{\mu} (1 + B_{(\mu)}) \tilde{p}_{F,(\mu)},$$

or, using Equation (C6),

$$\tilde{p} = \sum_{\mu} \tilde{p}_{(\mu)} = \sum_{\mu} (1 + B_{(\mu)}) (1 - \tilde{c}_{e,(\mu)}^2 \tilde{\nu}_F^2)^{-1} \tilde{\Theta}_{(\mu)}. \quad (\text{C8})$$

Here $B_{(\mu)} = B_{(\mu)}(\tilde{r})$ is a function describing the homogeneous solutions needed to meet the boundary conditions (see Appendix C.2.1 for an explicit example). It is written in a form that conveniently presents the boundary effects as a factor modifying the particular solution to provide the complete solution. When $\|B_{(\mu)}\| \ll 1$, the full solution converges with that of simply the particular solution $\tilde{p}_{F,(\mu)}$ where resonant amplification is controlled by simply the factor $(1 - \tilde{c}_{e,(\mu)}^2 \tilde{\nu}_F^2)^{-1}$. Note that the particular solution can be estimated from even rough knowledge of the interior parameters A_2 , A_1 , and A_0 , whereas $B_{(\mu)}$ sensitively depends on the interior structure and assumed boundary conditions. For understanding the vertical structure of the complete solution, one obviously needs to prescribe $B_{(\mu)}$ well. If one does not have a reliable prescription for $B_{(\mu)}$ but is interested in simply a basic estimate of tidal power, resonance, and scattering, the particular solution may be used to

provide an estimate for \tilde{p} . The justification is that for most cases it will be unlikely that it happens to be that $B_{(\mu)} \approx -1$ throughout the depth such that the power estimate using the particular solution would be an overestimate. If, in fact, $\|B_{(\mu)}\| \gg 1$, the power will have been underestimated. The boundary effect factor $(1 - B_{(\mu)})$ reveals the possibility of additional boundary resonances (e.g., when C_B , defined in Appendix C.2.1, is small) that can lead to local large amplitudes near the boundaries or propagating into the interior. Because $B_{(\mu)}$ varies with the spatial scale of the μ th mode, the boundary effect will also act as a filter distorting the spectral energy representation even in the interior.

The description above requires that the coefficients A_2 , A_1 , and A_0 be constant or slowly varying. If this is not valid, one can seek a transformation of \mathcal{L}_V or a variation of parameters such that a new set of coefficients is presented that may vary more slowly. This is described in Appendix C.2.2.

C.2.1. Boundary Condition Function $B_{(\mu)}$

Depending on the vertical structure of the fluid assumed, the operator \mathcal{L}_V may involve up to second order differentiation with respect to the radial coordinate. Therefore, there are up to two homogenous solutions \tilde{p}_{h1} , \tilde{p}_{h2} (with the radial dependencies $\tilde{r}^{q_{h1}}$, $\tilde{r}^{q_{h2}}$), which must be added to the particular solution to satisfy boundary conditions at \tilde{r}_1 , \tilde{r}_2 . These boundary conditions are written here in the generic form

$$c_1(\tilde{r} = \tilde{r}_1)\tilde{p}_{h1}(\tilde{r} = \tilde{r}_1) + c_2(\tilde{r} = \tilde{r}_1)\tilde{p}_{h2}(\tilde{r} = \tilde{r}_1) = -\tilde{p}_F(\tilde{r} = \tilde{r}_1), \quad (C9)$$

$$c_3(\tilde{r} = \tilde{r}_2)\tilde{p}_{h1}(\tilde{r} = \tilde{r}_2) + c_4(\tilde{r} = \tilde{r}_2)\tilde{p}_{h2}(\tilde{r} = \tilde{r}_2) = -\tilde{p}_F(\tilde{r} = \tilde{r}_2), \quad (C10)$$

where the functions $c_{(i)}$ can be chosen to reflect Dirichlet, Neumann, or Robin boundary conditions.

Assuming \mathcal{L}_V as described in Appendix C.2 with constant A_2 , A_1 , and A_0 , these equations can also be written in terms of the variables at arbitrary \tilde{r} (i.e., in terms of $\tilde{p}_{h1}(\tilde{r})$, $\tilde{p}_{h2}(\tilde{r})$, $\tilde{p}_F(\tilde{r})$) as

$$\left(c_1(\tilde{r} = \tilde{r}_1) \left(\frac{\tilde{r}}{\tilde{r}_1} \right)^{q_F - q_{h1,(\mu)}} \right) \tilde{p}_{h1} + \left(c_2(\tilde{r} = \tilde{r}_1) \left(\frac{\tilde{r}}{\tilde{r}_1} \right)^{q_F - q_{h2,(\mu)}} \right) \tilde{p}_{h2} = -\tilde{p}_F, \quad (C11)$$

$$\left(c_3(\tilde{r} = \tilde{r}_2) \left(\frac{\tilde{r}}{\tilde{r}_2} \right)^{q_F - q_{h1,(\mu)}} \right) \tilde{p}_{h1} + \left(c_4(\tilde{r} = \tilde{r}_2) \left(\frac{\tilde{r}}{\tilde{r}_2} \right)^{q_F - q_{h2,(\mu)}} \right) \tilde{p}_{h2} = -\tilde{p}_F, \quad (C12)$$

and then solved to give

$$\tilde{p}_{h1,(\mu)} = B_{1,(\mu)} \tilde{p}_F, \quad (C13)$$

$$\tilde{p}_{h2,(\mu)} = B_{2,(\mu)} \tilde{p}_F, \quad (C14)$$

where the functions

$$B_{1,(\mu)} = \frac{\left(c_2(\tilde{r} = \tilde{r}_1) \left(\frac{\tilde{r}}{\tilde{r}_1} \right)^{q_F - q_{h2,(\mu)}} \right) - \left(c_4(\tilde{r} = \tilde{r}_2) \left(\frac{\tilde{r}}{\tilde{r}_2} \right)^{q_F - q_{h2,(\mu)}} \right)}{C_B}, \quad (C15)$$

$$B_{2,(\mu)} = \frac{\left(c_3(\tilde{r} = \tilde{r}_2) \left(\frac{\tilde{r}}{\tilde{r}_2} \right)^{q_F - q_{h1,(\mu)}} \right) - \left(c_1(\tilde{r} = \tilde{r}_1) \left(\frac{\tilde{r}}{\tilde{r}_1} \right)^{q_F - q_{h1,(\mu)}} \right)}{C_B}, \quad (C16)$$

with

$$C_B = \left(c_1(\tilde{r} = \tilde{r}_1) \left(\frac{\tilde{r}}{\tilde{r}_1} \right)^{q_F - q_{h1,(\mu)}} \right) \left(c_4(\tilde{r} = \tilde{r}_2) \left(\frac{\tilde{r}}{\tilde{r}_2} \right)^{q_F - q_{h2,(\mu)}} \right) - \left(c_3(\tilde{r} = \tilde{r}_2) \left(\frac{\tilde{r}}{\tilde{r}_2} \right)^{q_F - q_{h1,(\mu)}} \right) \times \left(c_2(\tilde{r} = \tilde{r}_1) \left(\frac{\tilde{r}}{\tilde{r}_1} \right)^{q_F - q_{h2,(\mu)}} \right). \quad (C17)$$

The total $B_{(\mu)}$ is then $B_{(\mu)} = B_{1,(\mu)} + B_{2,(\mu)}$.

C.2.2. Variation of Parameters

Consider the governing Equation (C5). If the coefficients A_2 , A_1 , and A_0 are not constant or slowly varying, one may transform the equation into one involving new coefficients. Considering an arbitrary function $\xi = \xi(\tilde{r})$, Equation (C5) may be rewritten as

$$[I - [\mathcal{L}_H][C_2 \tilde{\partial}_r \tilde{\partial}_r + C_1 \tilde{\partial}_r + C_0]] \{\xi^{-1} \tilde{p}\} = \xi^{-1} \tilde{\mathfrak{G}}, \quad (C18)$$

where $C_2 = A_2$, $C_1 = 2A_2 \tilde{\partial}_r \ln \xi + A_1$, $C_0 = A_2 \tilde{\partial}_r \tilde{\partial}_r \ln \xi + (A_2 \tilde{\partial}_r \ln \xi + A_1) \tilde{\partial}_r \ln \xi + A_0$.

Because ξ is arbitrary, there is much potential for altering the coefficients into more slowly varying forms. One may also choose ξ such as to remove one of the terms. Most notably, one may remove the first-order differential term. By choosing $\xi = e^{-\frac{1}{2} \int \frac{A_1}{A_2} d \ln r}$, Equation (C18) becomes

$$[I - [\mathcal{L}_H][D_2 \tilde{\partial}_r \tilde{\partial}_r + D_0]] \{\xi^{-1} \tilde{p}\} = \xi^{-1} \tilde{\mathfrak{G}}, \quad (C19)$$

where $D_2 = A_2$, and $D_0 = A_2 \left(-\frac{1}{2} \tilde{\partial}_r \left\{ \frac{A_1}{A_2} \right\} - \frac{1}{4} \frac{A_1^2}{A_2^2} + \frac{A_0}{A_2} \right)$. While A_2 , A_1 , and A_0 are defined in terms of Υ_1 , Υ_2 , $\Upsilon_3 \chi_1$, and χ_2 in Appendix A.1.1, note that the ratios appearing here can be written compactly as $\frac{A_1}{A_2} = \tilde{\partial}_r \{\ln \Upsilon_2\} + \chi_1 + \chi_2$,

and $\frac{A_0}{A_2} = \chi_2 \tilde{\partial}_r \ln \{\Upsilon_2 \chi_2\} + \chi_1 \chi_2 + \Upsilon_1^{-1} \Upsilon_2^{-1} \Upsilon_3$. Recall that Υ_1 , Υ_2 , $\Upsilon_3 \chi_1$, and χ_2 are the coefficients appearing in the generic description of \mathcal{L}_V in Equation (A6), and these are related to the specific physical parameters for Jupiter in Appendix A.1.1.

References

- Auclair-Desrotour, P., Laskar, J., & Mathis, S. 2016, [A&A](#), **603**, A107
Duer, K., Galanti, E., & Kaspi, Y. 2020, [JGRE](#), **125**, e06292
French, M., Becker, A., Lorenzen, W., et al. 2012, [ApJS](#), **202**, 5
Galanti, E., & Kaspi, Y. 2021, [MNRAS](#), **501**, 2352
Hough, S. 1898, [RSPT](#), **191**, 139
Idini, B., & Stevenson, D. J. 2021, [PSJ](#), **2**, 69
Ingersoll, A. P., Adumitroaie, V., Allison, M. D., et al. 2017, [GeoRL](#), **44**, 7676
Ingersoll, A. P., Dowling, T., & Gierasch, P. 2004, in *Jupiter. The Planet, Satellites and Magnetosphere*, ed. F. Bagenal, T. E. Dowling, & W. B. McKinnon (Cambridge: Cambridge Univ. Press), 105
Ioannou, P. J., & Lindzen, R. S. 1993a, [ApJ](#), **406**, 252
Ioannou, P. J., & Lindzen, R. S. 1993b, [ApJ](#), **406**, 266
Ioannou, P. J., & Lindzen, R. S. 1994, [ApJ](#), **424**, 1005
Johnson, P. E., Morales-Juberías, R., Simon, A., et al. 2018, [P&SS](#), **155**, 2

- Kaspi, Y., Galanti, E., Hubbard, W. B., et al. 2018, *Natur*, **555**, 223
- Lainey, V., Arlot, J.-E., Karatekin, A., & Hoolst, T. V. 2009, *Natur*, **459**, 957
- Li, L., Jiang, X., West, R. A., et al. 2018, *NatCo*, **9**, 3709
- Lindzen, R. 1991, *GApFD*, **58**, 123
- Ni, D. 2018, *A&A*, **613**, A32
- Sánchez-Lavega, A. 2011, *An Introduction to Planetary Atmospheres* (Boca Raton, FL: CRC Press)
- Tyler, R. H. 2019a, Tidal Response Of Planetary Fluids (TROPF), Tech. rep., <https://github.com/RobertHTyler/TROPF>
- Tyler, R. H. 2019b, *P&SS*, **165**, 244
- Wahl, S. M., Hubbard, W. B., & Militzer, B. 2016, *ApJ*, **831**, 14
- Wahl, S. M., Parisi, M., Folkner, W. M., Hubbard, W. B., & Militzer, B. 2020, *ApJ*, **891**, 42
- Whitmell, C. T. 1899, *JBAA*, **10**, 66